Area Efficient D/A Converters For Accurate DC Operation

by

Brandon Royce Greenley

A THESIS

submitted to

Oregon State University

in partial fulfillment of
the requirements for the
degree of

Master of Science

Presented May 31, 2001
Commencement June 2002

ACKNOWLEDGMENT

TABLE OF CONTENTS

TABLE OF CONTENTS (Continued)

LIST OF FIGURES

AREA EFFICIENT D/A CONVERTERS FOR ACCURATE DC OPERATION

1. INTRODUCTION

Digital to analog conversion is one of the common functions in modern communications and other mixed-signal systems [1, 2, 3]. Decoding a digitally processed signal into a form that can be played out of a loudspeaker or transmitted by an antenna requires a digital to analog converter (DAC). While DACs have been used since the invention of the digital computer, designers are continuously introducing new and more complex systems in which DACs are needed. With increasing complexity comes an increase in the number of devices in a system, and hence, an increase in the die size required for that system. As the die space available becomes more and more critical, the need to optimize each function in the system for area consumption becomes a prime objective [4, 5, 6].

1.1 Motivation

Advancements in the wireless and mixed-signal areas have driven the integration of analog and digital systems on the same chip to never before seen levels. The integration is so pronounced that there are complete system on a chip solutions for several telecommunications applications [7, 8, 9]. As a circuit designer works to incorporate more functions onto the same chip, he often becomes more concerned with the area consumption of each individual circuit block.

At the same time that the levels of integration are increasing, the speed and complexity of mixed-signal systems is also growing rapidly [2, 10, 11, 12]. Many

mixed-signal systems require the use of circuits that operate at both high frequency and near DC. The critical circuits of a high speed data path will often be large and consume fairly large amounts of power. Often times these high speed circuits cannot be reduced in size or power because the performance would degrade below the required level. The low frequency circuits however, should be optimized for area and power consumption because the performance can often remain the same when size and power are reduced [13, 14].

Low frequency calibration circuits are widely used in the design of mixed-signal integrated circuits (ICs) to aid with the biasing of complex analog circuitry. These calibration circuits should be as small as possible so that the surrounding circuitry remains virtually unchanged in the layout. One common method for producing analog voltages and currents for biasing is to implement a small calibration DAC. The advantage of having a small DAC cell is that reference voltages and currents can be varied easily by a micro-controller until the proper analog bias is achieved.

The current age of portable electronic devices has also pushed designers to minimize power consumption as well as chip area. To help conserve the battery life of these portable devices, modern mixed-signal ICs are required to have a low power consumption, and hence, a low supply voltage. The work to be described herein focuses on a solution for a low voltage, area optimized calibration circuit in the form of a 10-bit DAC. In addition, a design for a 13-bit DAC is presented for applications requiring a higher resolution DC DAC.

1.2   Existing DAC Designs

There are many different architectures that have been used to implement DACs since their invention [15, 16, 17]. One of the most common DAC types is the current steering DAC. Three different variations of a 3-bit current steering DAC are shown

in Fig. 1.1. The simplest architecture is the binary weighted DAC, which uses a set of binary weighted current sources and resistors to correctly scale the branch currents. These currents will be switched to some output node above the current sources by a set of switches. The R-2R ladder DAC works with a similar principle to the binary weighted DAC. The current sources are binary weighted, but the resistors are implemented in a string such that the currents divide proportionally. All the resistors have the same value which increases the R-2R's effectiveness for implementation. The third architecture shown in Fig. 1.1 is the thermometer coded DAC. The thermometer DAC uses some decoding logic to switch in an additional current source of the same value each time there is an increase in the digital input.

Most of the recently published DACs are a combination of the three basic architectures listed above [1, 2, 10, 11, 18, 19, 20]. A segmented DAC is one in which the architecture is composed of more than one basic style. Since the thermometer architecture has many desirable features, it is quite common to use this architecture for the most significant bits (MSBs), while utilizing a more area efficient architecture (like the binary or R-2R) for the least significant bits (LSBs) where errors can be more easily tolerated.

Much of the current focus of DAC research has come in the area of high speed, high resolution DACs. A great deal of time has been spent investigating the
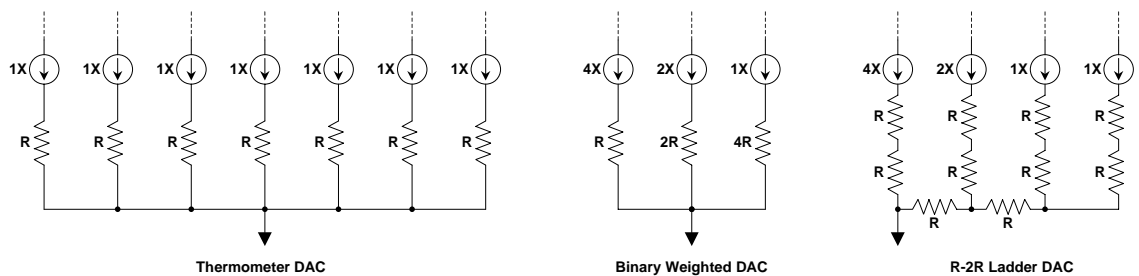
FIGURE 1.1: Popular DAC Designs.

dynamic behavior of DACs and how to increase the spurious free dynamic range (SFDR) [1, 2, 3, 10, 18, 21]. Other equally researched DAC problems are output glitching energy, clock feed-through, and the static specifications such as integral non-linearity (INL) and differential non-linearity (DNL) [11, 15, 20, 22].

With the exception of [2] and [5], all of the DACs referenced for this work consume well over 1 mm^2 of die area. Virtually all of the currently published DACs exceed 1 mm^2 area. The area consumed by most of these DACs is not deemed unreasonable because of their high speed and/or high resolution performance. However, this area would be unacceptable for a DAC that is not required to perform at high frequencies. With an interest in achieving high accuracy calibration DACs, and given the existing current steering DACs that show good results at high speeds, it is desirable to investigate architectures for which high performance DC DACs can be realized in a fraction of the area required for high speed DACs.

1.3 Research Objective

The work described herein will demonstrate that low voltage, highly accurate, DC DACs can be implemented in a standard digital CMOS process and consume minimal chip area. Both simulated and fabricated implementations of the architecture are used to verify the performance. Measurement results, combined with simulation results from SPICE and MATLAB prove the accuracy of operation.

This thesis provides a view that differs from current high speed DACs by exploring die area optimization and highly accurate low voltage DC operation. By implementing an ultra high gain op-amp for servoing, the DAC is capable of producing linear output currents with the output as high as 1.4V from a 1.8V power supply. The methods of DAC modeling and area optimization are demonstrated for 10-bit and 13-bit DAC designs, but could be applied to any DC DAC design.

2. BASIC CONCEPTS AND FIGURES OF MERIT FOR DACS

Before describing the designs, simulations, and results, the basic concepts surrounding digital to analog conversion need to be reviewed. An overview of the operation and performance measurements of digital to analog converters will be presented in this chapter. Both static and dynamic operation will be discussed along with the key figures of merit for each type of DAC operation.

2.1   Static Performance Measures

Historically, the figures of merit that have received the most attention for DACs are the static ones [2, 11]. The most common static figures of merit are integral non-linearity (INL), differential non-linearity (DNL), and monotonicity. DACs also commonly exhibit other characteristics that are not as frequently mentioned; namely offset error and gain error. Figure 2.1 shows an input/output transfer curve for a 2-bit DAC. Both gain error an offset error are depicted in Fig. 2.1, with the ideal transfer curve shown as a reference. It can be seen that the offset error is merely a shift up or down of the entire curve. The gain error on the other hand can have points in common with the ideal curve at the beginning or end, but the gain error curve has a different slope than the ideal. The reason that these DAC characteristics are not commonly mentioned is because they are easily corrected for, and often cause no problems in certain applications even if they are not corrected [15]. Before measuring INL, DNL, or monotonicity, it is assumed that both the gain error and offset error have been corrected, so that ideal transfer curve becomes the reference once again.

Figure 2.2 shows a typical non-linear DAC response. The non-linear curve
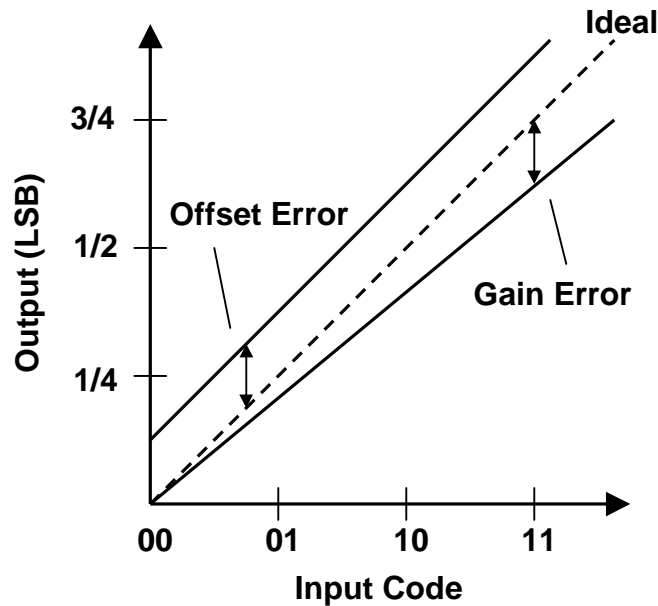
FIGURE 2.1: 2-Bit Input/Output DAC Transfer Curve.

has been normalized so that the endpoints of the curve line up with the endpoints of the ideal curve. This method of calculating INL is called the endpoint method [15]. INL is calculated as the difference between the actual response, and the ideal response. The INL is usually expressed in units of LSBs rather than absolute units.

$$INL = \frac{ActualValue - IdealValue}{IdealStep} \quad (LSB)$$

A different value of INL is recorded at each value of the input code, however a typical DAC data sheet may only quote one value for the INL. When only one value of INL is quoted, it is implied that this is the worst case INL throughout the entire input code range.

Figure 2.3 shows an actual 2-bit DAC response. Each time that the digital input code is increased by one LSB, the output should correspondingly increase by
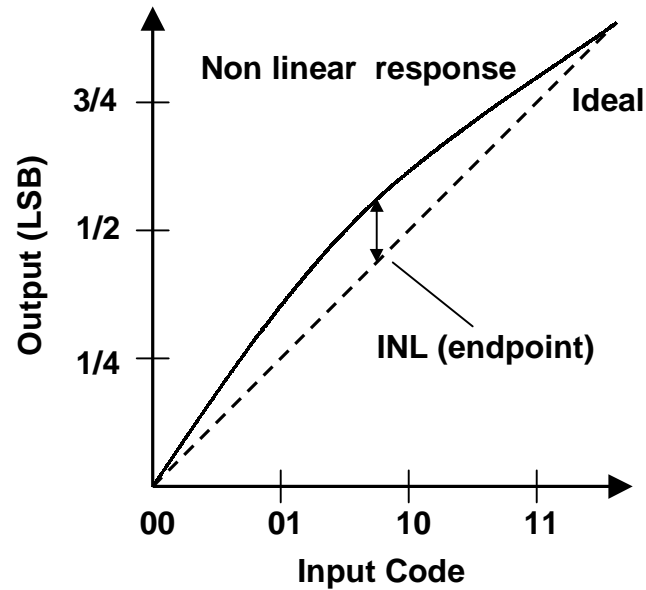
FIGURE 2.2: Non-linear Response Showing Endpoint INL Method.

one LSB. This ideal step is shown at the change from the 00 to 01 input codes. As the input changes from 01 to 10, the step size is larger than the ideal step. The difference between the actual step size and the ideal step size is the DNL. Just as with the INL, the DNL is represented in units of LSBs.

$$DNL = \frac{ActualStep - IdealStep}{IdealStep} \quad (LSB)$$

In the case of the 01 to 10 transition, the DNL is positive because the actual step is larger than the ideal. If the transition had caused the output to increase by less than one LSB, then the DNL would have been negative.

Monotonicity is defined by the output always incrementing by a non-negative amount as the input code increases [16]. As shown in Fig. 2.3, the transition from 10 to 11 causes the output to decrease rather than increase. Anytime this condition occurs, the DAC is said to be non-monotonic. It is often very desirable to have
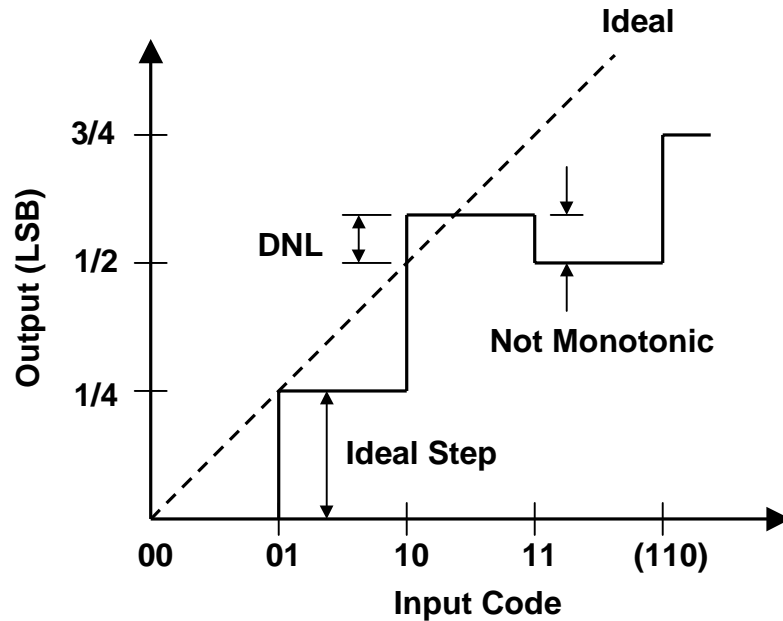
FIGURE 2.3: 2-Bit DAC Response Defining DNL and Monotonicity.

a DAC be monotonic. Depending on the application, the monotonic condition is often more important than either the INL or DNL [23]. A DAC is guaranteed to be monotonic if the worst case DNL is greater than -1 LSB.

2.2 Dynamic Performance Measures

As the performance of telecommunications systems becomes more demanding of DACs, the dynamic figures of merit become a critical element in system performance. The most common dynamic figures of merit are the update rate and the spurious free dynamic range (SFDR). As a matter of practice, these two measurements are inversely proportional. As the update rate (also referred to as sample rate in a Nyquist converter) goes higher, the SFDR lowers. The design goal of a high speed DAC is to have the highest possible update rate for a given SFDR spec-
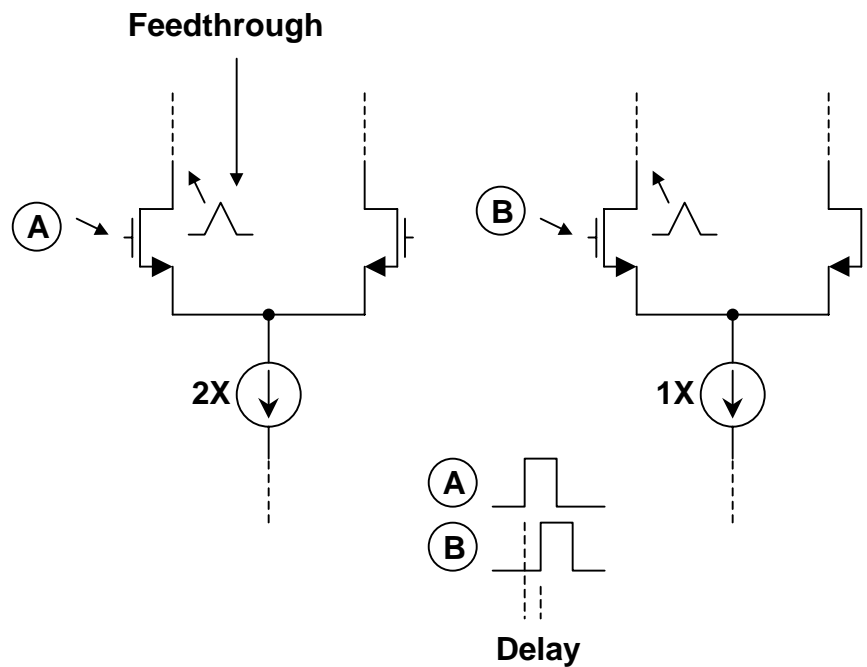
Feedthrough

FIGURE 2.4: DAC Switches With Clock Feed-through and Control Signal Latency.

ification. There are many factors that limit the dynamic performance of a DAC, but the two major ones are: timing latency between control signals at the switches, and coupling of the control (clock) signals through the parasitic capacitance of the switch into the circuit [2, 11].

Figure 2.4 shows two control signals labeled A and B that should arrive at the gates of the corresponding switches at the same time. The timing diagram in the figure shows that signal B is actually slightly delayed from signal A. Latency between the control signals as shown will have a direct negative effect on the dynamic performance of a DAC. Figure 2.4 also shows a small triangle pulse at the drain of the switches. This signal represents a portion of the clock signal that gets coupled through the gate-drain capacitance of the switch, directly into the circuit. Just as in the signal latency case, the effect of clock feed-through will have a direct negative impact on the dynamic performance of a DAC.

3. DAC DESIGN

Now that the concepts behind digital to analog conversion have been introduced the proposed 10-bit DAC is presented in detail. The DAC architecture is segmented to utilize the performance advantages of thermometer coding on the MSBs, while capitalizing on the area savings of the R-2R ladder for the LSBs. The optimization of die area that resulted in the chosen architecture is discussed in detail. A device mismatch analysis was performed in MATLAB to arrive at the implemented design. A method for providing linear output currents from the DAC, while at the same time overcoming the limitations proposed by the 1.8 V power supply, will be presented. The design of the digital circuitry to control the switches will be briefly explained before simulation results from MATLAB and SPICE are presented. The detailed process guidelines of a standard digital $0.18\,\mu$m CMOS process have been carefully considered to ensure DAC performance with temperature and process variations. Figure 3.1 shows a simplified block diagram for the system.

3.1 Architecture Design

In virtually all aspects of DAC design, there is one particular architecture which dominates the performance of all others. The thermometer coded current steering DAC (Fig. 1.1) is the one in which there are $2^N - 1$ current sources in a N-Bit DAC. This architecture has a separate current source for each of the 2^N different input bits. The thermometer DAC is guaranteed to be monotonic because each time the input code is increased, another current source is added, and none of the current sources that were on for the previous code turn off. The thermometer DAC also consumes more area than the other DAC architectures. The reason it

FIGURE 3.1: System Block Diagram.

consumes a large area is because the digital decoding logic needed to convert from a binary input code into a thermometer code becomes very large when the DAC has a resolution above 5 or 6 bits.

The DAC design presented in this work uses a segmented architecture where the upper three bits are implemented in a thermometer style, while the lower 6 bits are implemented with a R-2R ladder (Fig. 3.2). Using a thermometer architecture for the upper three bits maximizes performance where it is most critical while the R-2R ladder DAC has good performance while occupying a minimal amount of die area. In between the thermometer portion (M7-M13) and the R-2R portion (M0-M5), there exists a binary weighted branch, M6. A typical thermometer plus R-2R architecture would include the branch of M6 in the R-2R ladder, hence placing 2 resistors in the M6 branch and adding a resistor between the M5 and M6 branches. Such a typical approach would only require one resistor per branch for the thermometer portion. Figure 3.2 shows that the thermometer branches (M7-M13) have 2 resistors in parallel for each branch (R/2). With two resistors per branch, the matching of the resistors in the thermometer portion can be improved because the

effect of a linear process gradient can be eliminated by proper layout. Hence the reason that the middle branch (M6) is binary weighted rather than included in the R-2R portion.

Since this DAC operates from a single 1.8V power supply, the amount of headroom left above the current steering circuitry is not sufficient for providing output currents in a general application DAC. This low voltage limitation created the design of the current mirror output circuit. The output currents are shown as I_1 and I_2 in Fig. 3.2. The goal of the design is to achieve a linear and monotonic output current while supplying maximum voltage headroom. By mirroring currents off Mx1 and Mx2, the output nodes may be placed as high as 1.4V and still achieve linear operation. The gate voltage is produced from the servoing op-amps shown in Fig. 3.2. The servoing operation is an essential step in the functionality of the DAC. The servo maintains a constant voltage (V_{ref}) at the drains of Mx1 and Mx2, regardless of the currents passing through them. If the output nodes are set to the same V_{ref} voltage, then the output currents I_1 and I_2 will be a perfectly linear replica of the currents in Mx1 and Mx2. Servoing is the ideal solution to the headroom problem associated with the low voltage supply because the drain voltages of Mx1 and Mx2 remain more stable than for a bipolar device, and the servo provides the current mirror voltage at the same time.

3.2   Mismatch Modeling for Architectural Optimization

At this point only DAC architectures with resistors present in the current branches have been discussed, however the majority of the current steering DACs recently published have been implemented without the use of resistors [2, 5, 11, 19, 20, 21]. An analysis was performed in MATLAB to examine the effects of adding resistors below the current sources, and what effect device mismatch has on the
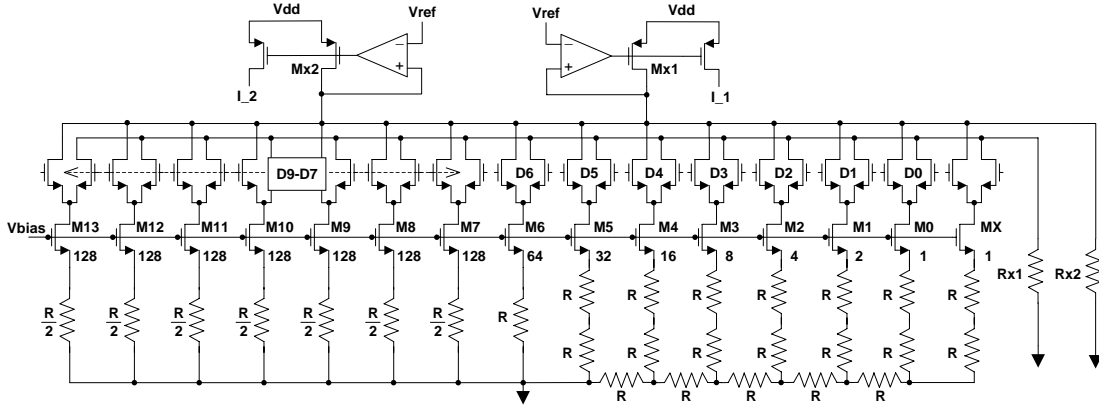
FIGURE 3.2: Schematic of Implemented DAC.

performance of the DAC. Figure 3.3 shows a schematic of the implemented DAC without the resistors. In this way, the lower portion of the DAC (M0-M6) acts as a simple binary weighted current steering DAC. The functionality of the DAC in Fig. 3.3 will be exactly the same as the DAC of Fig. 3.2. These two designs were modeled in MATLAB using matrices to represent the current source array and resistor array exactly as they appear in the layout. Random mismatches were assigned to each individual element in the arrays (devices in the layout).

The variation associated with the active region of a transistor during fabrication was modeled as random W/L variation. The current source devices in each branch of the DAC (eg. M4, Fig. 3.3) are a parallel connection of a certain number unit current source elements. These individual elements are NMOS transistors that are arranged in an array containing 1024 total elements (excluding dummy devices). Random variations of size (W/L) and threshold voltage (V_T) were assigned to each one of these individual elements in MATLAB. To show the modeling of random variations in W/L, M2 is used as an example. In M2, there are 4 unit elements tied in parallel to create one effective branch current source. The effective W/L for the device M2 is denoted as $(W/L)_{M2}$ while the W/L for the individual unit elements

FIGURE 3.3: No-Resistor DAC (Typical Current Steering DAC).

are denoted as $(W/L)_1$, $(W/L)_2$, $(W/L)_3$, and $(W/L)_4$. It can be seen that:

$$\left(\frac{W}{L}\right)_{M2} = \left[\left(\frac{W}{L}\right)_1 + \epsilon_1\right] + \left[\left(\frac{W}{L}\right)_2 + \epsilon_2\right] + \left[\left(\frac{W}{L}\right)_3 + \epsilon_3\right] + \left[\left(\frac{W}{L}\right)_4 + \epsilon_4\right]$$

where ϵ represents the error width that corresponds to a fraction of the nominal device W/L. This analysis for random W/L variation holds for all the branch current sources (M0-M13).

The random variation associated with V_T is considerably more complicated to model, and the model changes depending on which architecture is being analyzed. The most straightforward analysis of the no-resistor DAC (Fig. 3.3) will be examined first. To see how the individual V_T mismatches effect the branch currents, it is necessary to examine how the model calculates the currents. For simplicity M1 will be used as an example, and then a general expression will be extrapolated. Using the first order approximation for current in a NMOS transistor operating in the saturation region, it can be shown that:

$$I_{M1} = \frac{1}{2}k\left(\frac{W}{L}\right)_{M1}(V_{GS} - V_{TM1})^2 = k_n\left(\frac{W}{L}\right)_1(V_G - V_{T1})^2 + k_n\left(\frac{W}{L}\right)_2(V_G - V_{T2})^2$$

Where k_n is equal to: $k_n = \frac{1}{2}k = \frac{1}{2}\mu_n C_{ox}$. Multiplying through and expanding;

$$I_{M1} = k_n \left(\frac{W}{L}\right)_1 (V_G^2 - 2V_G V_{T1} + V_{T1}^2) + k_n \left(\frac{W}{L}\right)_2 (V_G^2 - 2V_G V_{T2} + V_{T2}^2)$$

Where: $V_{T1} = V_{Ti} + \epsilon_1$ and $V_{T2} = V_{Ti} + \epsilon_2$. This result for a branch current source with only two unit elements can be extrapolated to a general case that accommodates all the branch current sources (M0-M13).

$$I = k_n V_G^2 \sum_{j=1}^{2^N} \left(\frac{W}{L}\right)_j + k_n \sum_{j=1}^{2^N} \left(\frac{W}{L}\right)_j V_{Tj}^2 - 2V_G k_n \sum_{j=1}^{2^N} \left(\frac{W}{L}\right)_j V_{Tj}$$

Next, the branch currents for the resistor style DAC (Fig. 3.2) are solved. Since the source terminals of the current sources in the resistor DAC are not tied together at a common potential, the complexity of the model increases. Additional complexity is also added because the body effect of the unit elements was modeled for the current sources in this DAC. The threshold voltage for a unit element including the body effect is written as: $V_T = V_{TO} + \gamma \left(\sqrt{V_{SB} + |2\phi_F|} - \sqrt{|2\phi_F|}\right)$ where $\gamma = \sqrt{2qN_A K_S \epsilon_O}/C_{OX}$. Both γ and ϕ_F can be assumed as constants and taken directly from the process specifications. If γ and ϕ_F are both taken as constants, then the only variable upon which the body effect depends is the source-bulk potential, V_{SB}. Since the bulk of the NMOS device is the silicon substrate, and it is connected to ground, V_{SB} is simply the source voltage (V_S), and will be referred to as such from here on.

The model for the branch currents in the resistor DAC (Fig. 3.2) is different for current sources M5-M13 than it is for current sources MX-M4. This difference arises because the voltages between the resistors in the R-2R ladder are not known, and therefore need to be solved iteratively. For the resistors in the upper portion however, one side is tied to ground, and the analysis is simplified. The model for

the upper portion will be examined first. For simplicity of this derivation, current source M6 is assumed to have only 2 unit elements rather than 64, then a general equation is extrapolated which accurately models M5-M13.

$$I_{M6} = k_n \left(\frac{W}{L}\right)_1 (V_G - V_S - V_{T1})^2 + k_n \left(\frac{W}{L}\right)_2 (V_G - V_S - V_{T2})^2$$

Where: $V_S = IR$. Multiplying through and expanding;

$$I_{M6} = k_n \left(\frac{W}{L}\right)_1 [I^2 R^2 + 2V_{T1}IR - 2V_G IR + V_{T1}^2 + V_G^2 - 2V_G V_{T1}] + ...$$

$$k_n \left(\frac{W}{L}\right)_2 [I^2 R^2 + 2V_{T2}IR - 2V_G IR + V_{T2}^2 + V_G^2 - 2V_G V_{T2}]$$

Since the result is a quadratic function, the I terms are collected and the equation is set equal to zero. For simplicity, $k_n \left(\frac{W}{L}\right)_1$ is written as K_1 and $k_n \left(\frac{W}{L}\right)_2$ is K_2.

$$I^2(K_1 R^2 + K_2 R^2) + I(2K_1 V_{T1}R + 2K_2 V_{T2}R - 2K_1 V_G R - 2K_2 V_G R - 1) + ...$$

$$K_1(V_{T1}^2 + V_G^2 - 2V_G V_{T1}) + K_2(V_{T2}^2 + V_G^2 - 2V_G V_{T2}) = 0$$

Each term can be collected and represented generally as:

$$I^2 \text{ Term} = R^2 k_n \sum_{j=1}^{2^N} \left(\frac{W}{L}\right)_j$$

$$I \text{ Term} = 2Rk_n \sum_{j=1}^{2^N} \left(\frac{W}{L}\right)_j V_{Tj} - 2RV_G k_n \sum_{j=1}^{2^N} \left(\frac{W}{L}\right)_j - 1$$

$$\text{Constant Term} = V_G^2 k_n \sum_{j=1}^{2^N} \left(\frac{W}{L}\right)_j + k_n \sum_{j=1}^{2^N} \left(\frac{W}{L}\right)_j V_{Tj}^2 - 2k_n V_G \sum_{j=1}^{2^N} \left(\frac{W}{L}\right)_j V_{Tj}$$

These quadratic terms were used in MATLAB to solve the branch currents for M5-M13. The MATLAB model works iteratively to solve these branch currents because the branch current is dependent on V_T, and V_T is dependent on the source

voltage (V_S), which in turn, is dependent on the branch current and the resistance. The final DAC currents that need to be solved are the R-2R currents of MX-M4. In this derivation, M1 is used as an example. It can be seen that:

$$I_{M1} = k_n \left(\frac{W}{L}\right)_1 (V_G - V_{S1} - V_{T1})^2 + k_n \left(\frac{W}{L}\right)_2 (V_G - V_{S1} - V_{T2})^2$$

Multiplying through and expanding all squared terms;

$$I_{M1} = k_n \left(\frac{W}{L}\right)_1 [V_G^2 - 2V_G V_{S1} - 2V_G V_{T1} + 2V_{S1}V_{T1} + V_{T1}^2 + V_{S1}^2] + ...$$

$$k_n \left(\frac{W}{L}\right)_2 [V_G^2 - 2V_G V_{S1} - 2V_G V_{T2} + 2V_{S1}V_{T2} + V_{T2}^2 + V_{S1}^2]$$

Collecting all terms and extrapolating a general equation:

$$I_x = k_n[V_G^2 - 2V_G V_{Sx} + V_{Sx}^2] \sum_{j=1}^{2^N} \left(\frac{W}{L}\right)_j + 2k_n[V_{Sx} - V_G] \sum_{j=1}^{2^N} \left(\frac{W}{L}\right)_j V_{Tj} + k_n \sum_{j=1}^{2^N} \left(\frac{W}{L}\right)_j V_{Tj}^2$$

With both the resistor DAC of Fig. 3.2 and the no-resistor DAC of Fig. 3.3 accurately modeled in MATLAB, an analysis was performed to quantify the effects of device mismatch on DAC performance.

3.2.1   Resistor vs. No-Resistor Designs

Accurate modeling of the resistor and no-resistor DACs allowed for side by side comparison of the two architectures given a certain set of mismatch parameters. The three mismatch parameters: σ_W, σ_{V_T}, and σ_R are related to the parameters in the MATLAB model as follows: $\frac{W}{L} = \frac{W}{L}(1 + \sigma_W)$, $V_T = V_T(1 + \sigma_{V_T})$, and $R = R(1 + \sigma_R)$, where σ represents a normally distributed random number with zero mean and a variance of 1.0. Figure 3.4 shows the INL and DNL performance of
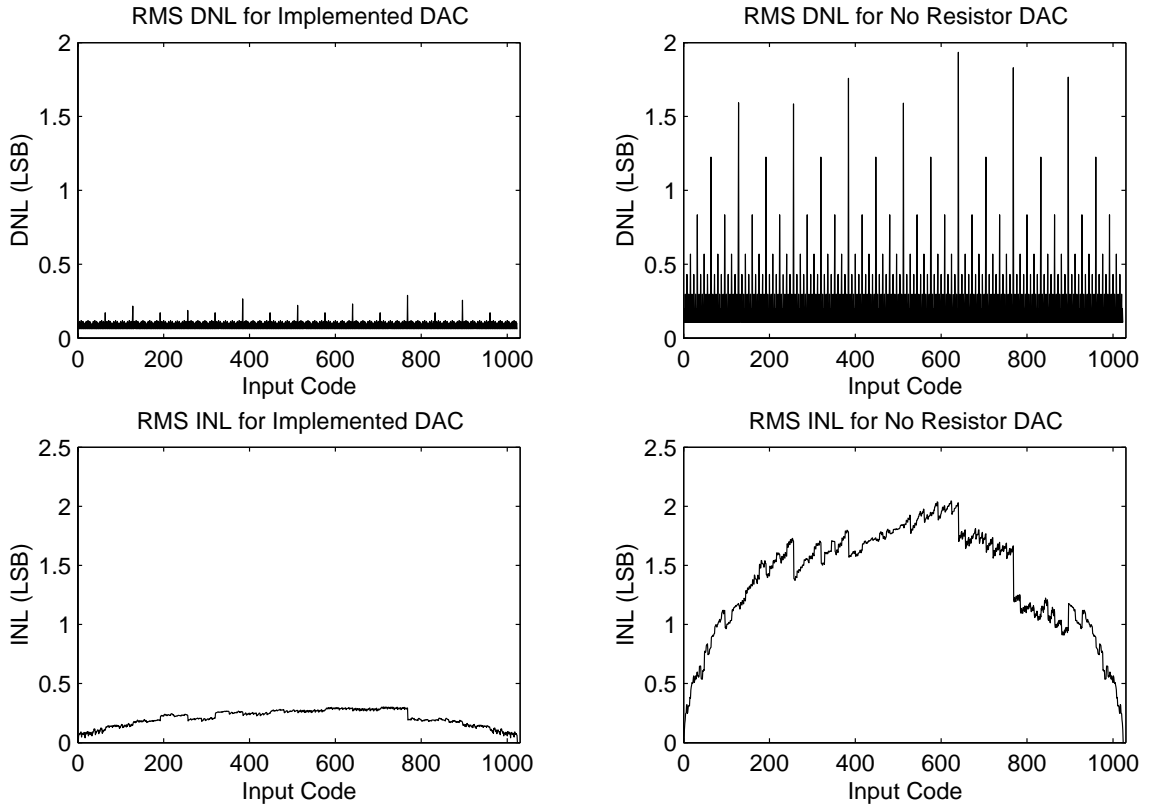
FIGURE 3.4: INL and DNL Performance of Resistor DAC and No-Resistor DAC.

each architecture for $\sigma_W = 0.005$, $\sigma_{V_T} = 0.005$, and $\sigma_R = 0.002$. Figure 3.4 clearly shows that when the matching of the resistors is more accurately controlled than the W/L and V_T variations, the performance of the resistor DAC is superior. Based on initial assumptions about the process, and past experience with similar CMOS processes, the conclusion was made to utilize the resistor style DAC because the resistor matching is predominately better than the transistor parameter matching.

The primary reason for the drastic difference seen in Fig. 3.4 relates directly to the derivations presented earlier in this section. The current in each branch of the resistor DAC (Fig. 3.2) is determined by a combination of the voltage across the resistors and the $\Delta (V_{GS} - V_T)$ of the current source transistors while the currents in the no-resistor DAC (Fig. 3.3) are determined only by the Δ of the current

source transistors. Therefore, as the matching of the resistors becomes better than the matching of the current source devices, the performance of the resistor DAC dominates. Likewise, as the voltage across the resistors becomes larger in the resistor DAC, the performance improves further. The area consumed by the resistors has to be carefully considered when deciding how large the voltage drop should be. In the design presented, the resistors were optimized to provide the best performance while consuming a minimal area.

3.2.2   Device Trade-Off Analysis

Once the decision was made to utilize resistors in the DAC, the architecture was optimized for area consumption. A trade-off analysis was performed to determine the number of devices needed for various DAC architectures. The number of resistors, switches, and digital decoding gates were analyzed to determine how many bits to implement with the thermometer code, and how many bits should be present in the R-2R ladder. If the entire 10 bits of the DAC were structured in a R-2R scheme, the upper four bits (D6-D9) would contain 12 resistors, 8 switches, and

Upper Bits	Element	R-2R	Implemented	Δ
3	resistors	9	7	-2
	switches	6	8	2
	gates	0	3	3
4	resistors	12	15	3
	switches	8	16	8
	gates	0	8	8
5	resistors	15	31	16
	switches	10	32	22
	gates	0	23	23

TABLE 3.1: Trade-off Analysis: Number of Bits In Thermometer Portion.

zero logic gates. In the segmented architecture that was implemented, the upper four bits contain 15 resistors, 16 switches and 8 logic gates.

Table 3.1 shows a summary of the number of resistors, switches, and 2-input logic gates needed to implement the upper 3, 4, or 5 bits. The binary bit that exists between the thermometer and R-2R portions of the implemented architecture is included in the 3, 4, or 5 bits examined in the table. Table 3.1 shows that the device increase from the full R-2R ladder to the implemented architecture is acceptable for 3 and 4 upper bits, but the increase in number of resistors, switches, and gates is not acceptable for 5 upper bits.

3.2.3   Switch and Device Sizing

The fundamental concept behind the design of this DAC is to allow for a predetermined amount of inherent error in order to achieve an optimally small area. The layout of the DAC determined the sizing of the current sources (M0-M13) and the switches directly above them in Fig. 3.2. Figure 3.5 shows the actual sizes of the switches and the currents associated with each branch. The minimum size switch, which is determined by the process, is $0.42\mu m/0.18\mu m$. If the switch
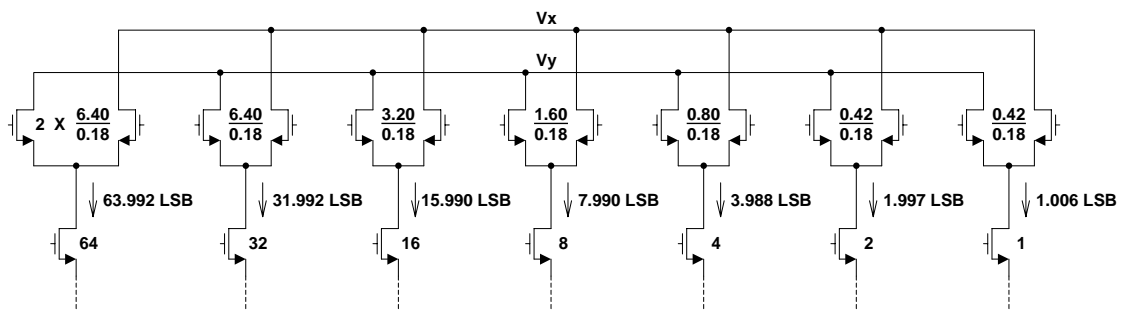

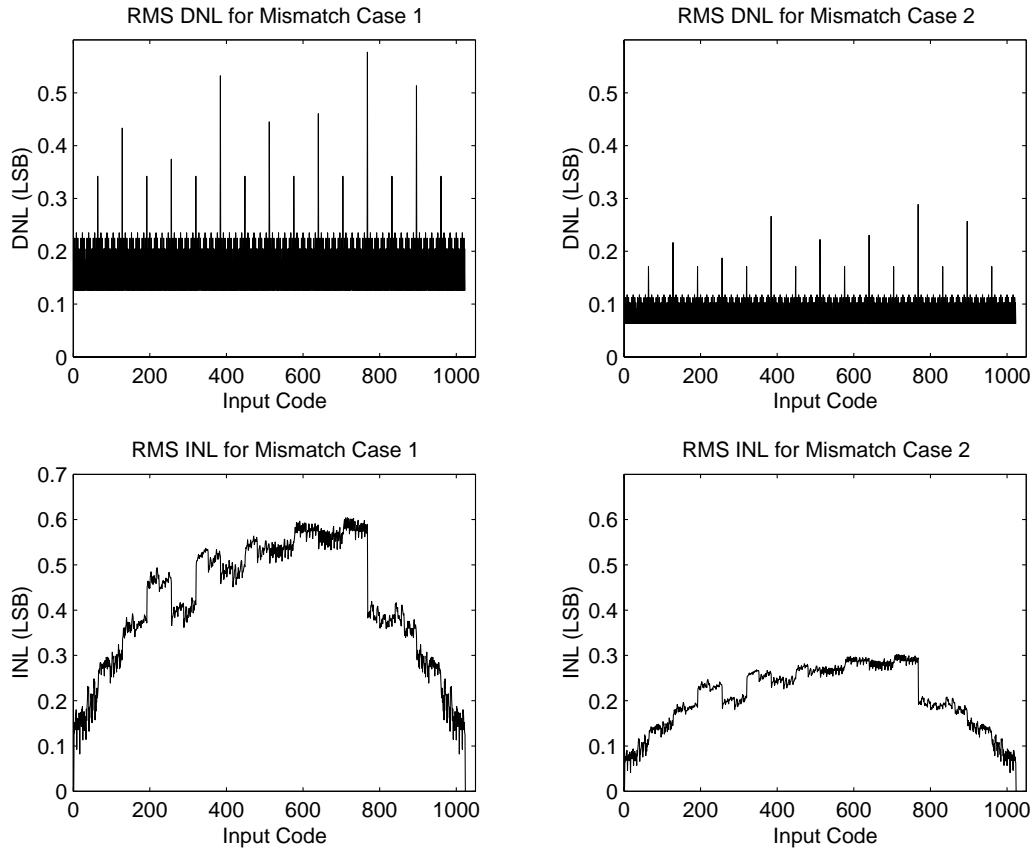FIGURE 3.5: Actual Branch Currents As a Result of Non-Ideal Switch Sizing.

FIGURE 3.6: Simulations of Mismatch in the Implemented Architecture.

sizing had been perfectly ideal, the switch above the 2X current source would be $2 \times 0.42\mu m/0.18\mu m$ rather than the implemented $0.42\mu m/0.18\mu m$ size. The errors caused by non-ideal scaling of these switches are present because each switch does not have the same voltage drop, and therefore the current sources do not have the same drain-source voltages (V_{DS}). The finite difference in V_{DS} for the current sources causes the currents in each branch to be slightly less than ideal, but still well within the predetermined error budget.

The current source and resistor sizes are also optimized for area and performance. Using the MATLAB models described at the beginning of this section, a series of Monte Carlo simulations were performed to analyze the effects of device mismatch on DAC performance. Figure 3.6 shows the results of two such simulations.
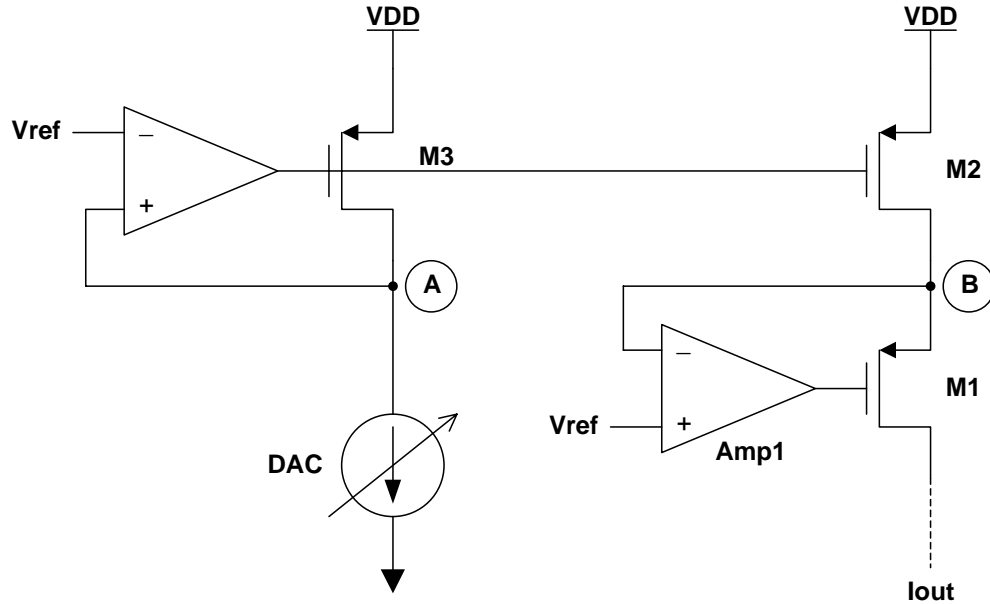
FIGURE 3.7: Simplified DAC Schematic With Linear Output Current Mirror.

Mismatch case 1 used the following parameter variations: $\sigma_W = 0.01$, $\sigma_{V_T} = 0.01$, and $\sigma_R = 0.004$; while mismatch case 2 used the following: $\sigma_W = 0.005$, $\sigma_{V_T} = 0.005$, and $\sigma_R = 0.002$. Although the expected matching from the process more closely correlates to case 2, Fig. 3.6 shows that even when the device mismatches are double the predicted values, the INL and DNL are well within the 10-Bit performance level.

3.3 Linear Output Current Mirror

The left side of Fig. 3.7 shows a simplified single ended version of the implemented DAC architecture. The variable current source represents the switches, current sources, and resistors. From the schematic of the actual DAC (Fig. 3.2), it can be seen that node B in Fig. 3.7 corresponds to either I_1 or I_2 in Fig. 3.2. The additional PMOS device (M1) and servoing op-amp (Amp1) shown in Fig. 3.7 create a linear output current that perfectly corresponds to the DAC current. Without
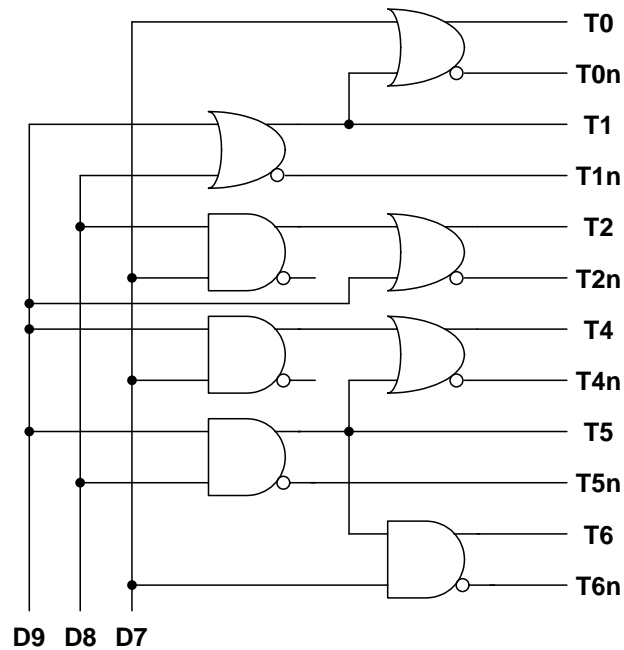
FIGURE 3.8: Decoding Logic For Binary to Thermometer Code.

these additional devices, node B would be free to change voltage depending on the output circuitry. Any variation in the voltage at node B will cause the currents in M2 and M3 to be slightly different, and hence will introduce non-linearity. The high gain servo created by Amp1 and M1, forces nodes A and B to the same voltage (Vref). The design of this output stage maintains a linear output current while the output node (Iout) is allowed to vary from 0V to 1.0 V, which is more than half of the available 1.8V power supply.

3.4   Digital Circuit Design

The digital circuitry needed for operation of the implemented DAC consists of a series of input latches, and decoding logic to transform the binary input code into thermometer code for D7-D9. The input latches act to hold the digital input
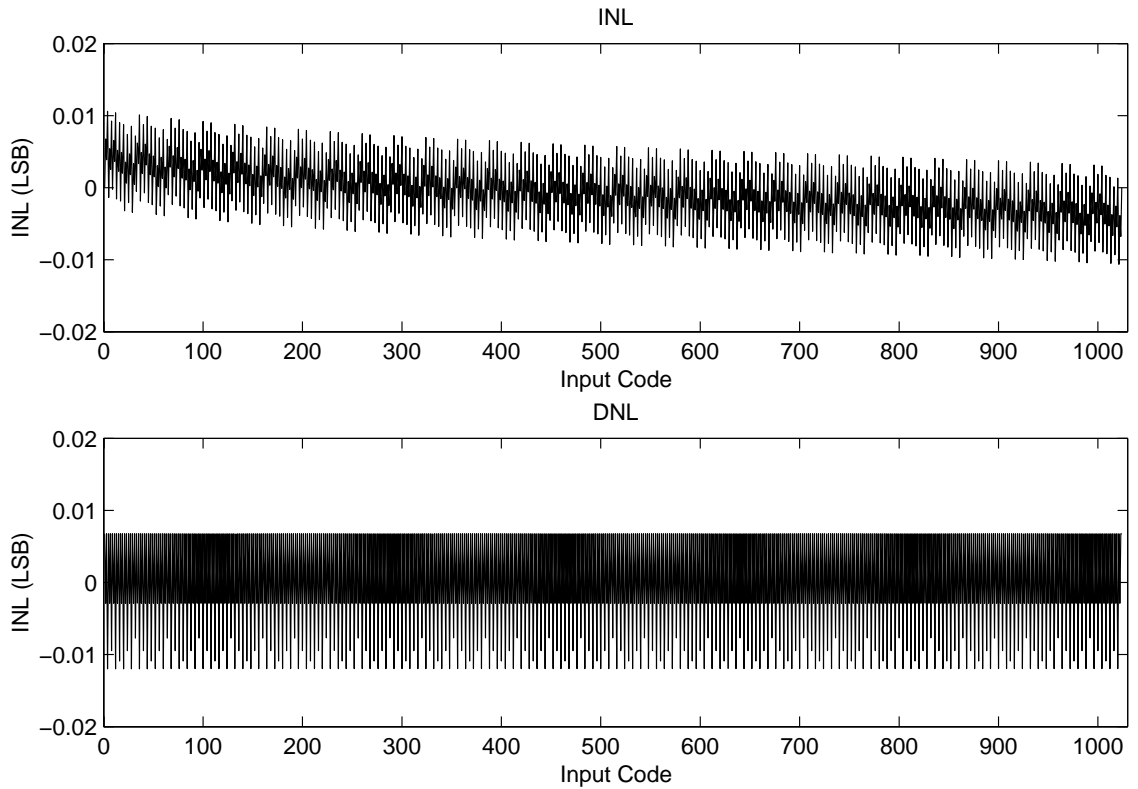
FIGURE 3.9: Simulated INL and DNL For Implemented 10-Bit DAC.

value at the inputs of the switches regardless of what is happening on the system digital bus. These latches are simple inverters connected back to back with a pass transistor. The decoding logic needed to transform the binary input code into a thermometer code is shown in Fig. 3.8. D7, D8, and D9 are the binary input bits, and T0-T6n are the differential thermometer code outputs. T0 and T0n correspond to branch M7, while T6 and T6n correspond to M13. T3 and T3n are not shown in Fig. 3.8 because they are equivalent to D9 and D9n. A minimum number of logic gates were used, and all the transistors that compose the actual gates are minimum sized devices in order to keep the area required to a minimum.
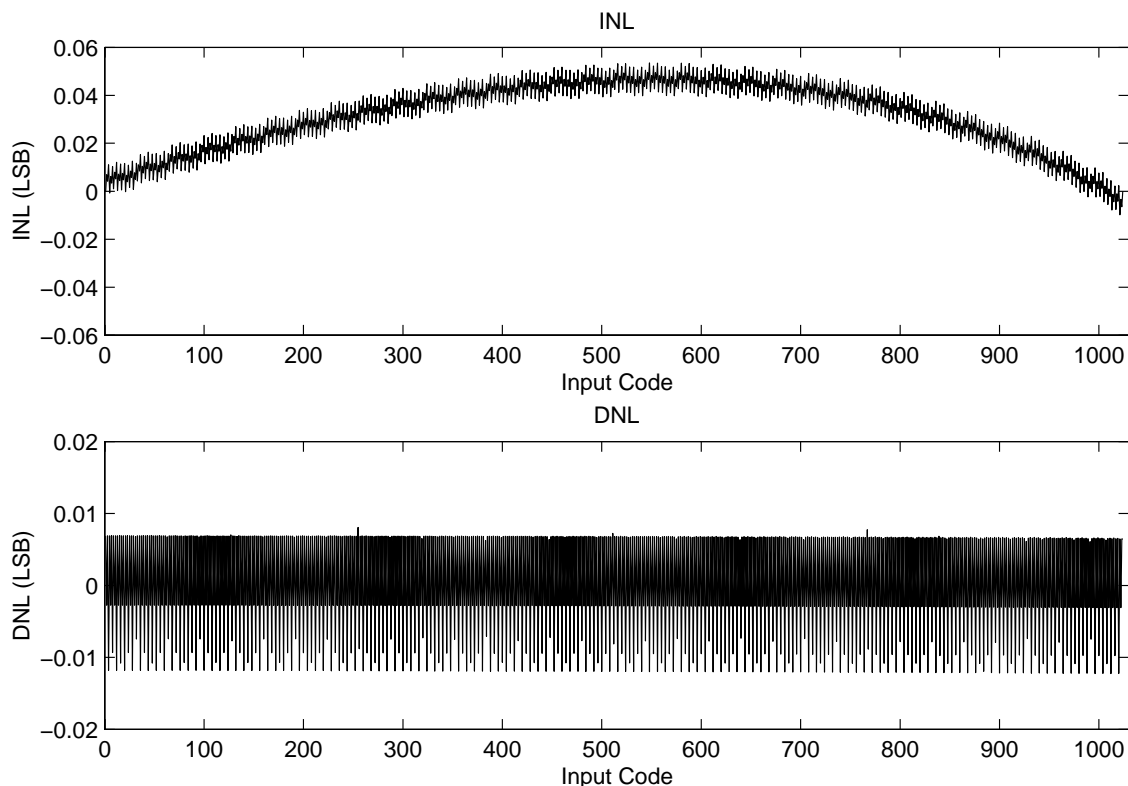
FIGURE 3.10: INL and DNL of Current Mirror Output With Finite Op-Amp Gain.

3.5 Simulation Results

Once the various DACs had been simulated and optimized in MATLAB to reach the optimal architecture, the DAC of Fig. 3.2 was designed using the results from SPICE simulations. Figure 3.9 shows the final DAC INL and DNL for the implemented design. Simulation results show that even with the slight error in branch currents due to non-ideal switch sizing, the INL and DNL are less than 0.02 LSB.

The linear output circuit described in the previous section did not discuss the effect of op-amp gain in the performance of the circuit. With infinite op-amp gain, the performance of the output circuit would exactly match the performance of the DAC core. Figure 3.10 shows the actual INL and DNL at the output of the
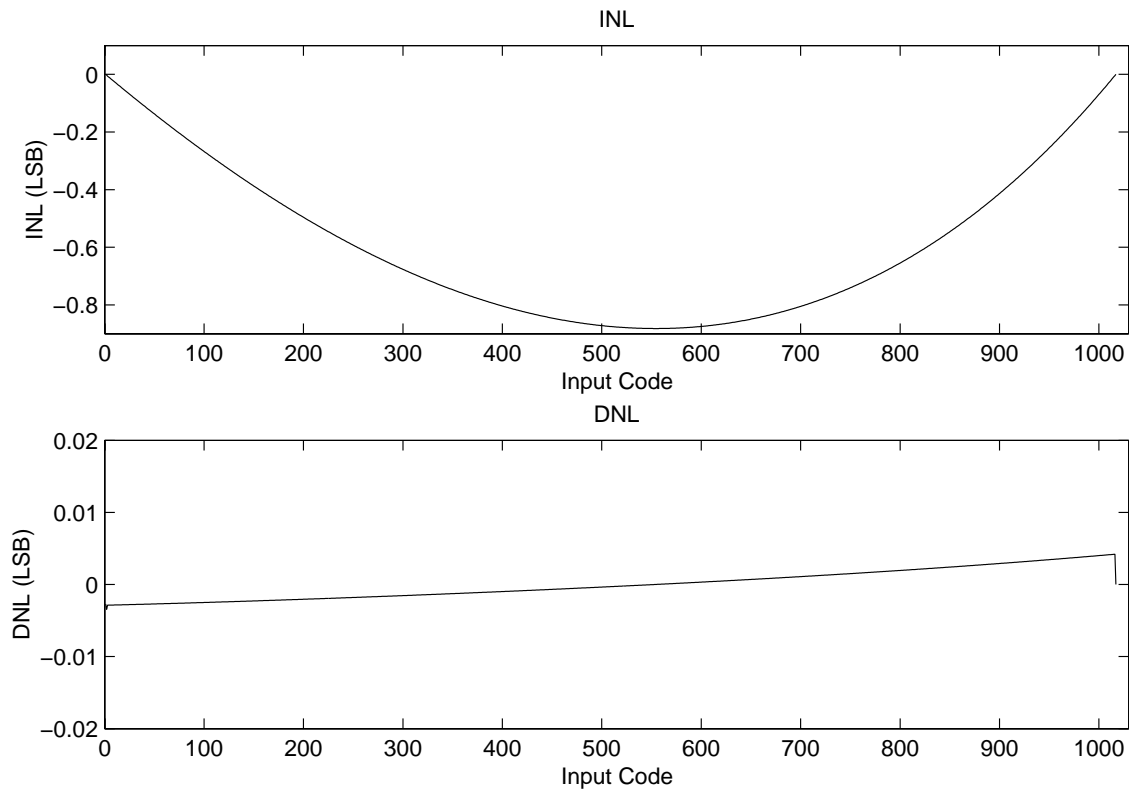
FIGURE 3.11: INL and DNL for Ideal Current Mirror With 10mV Offset.

mirroring circuit. The slight degradation in the simulated INL is present because of the finite op-amp gain in the output circuit. Since the gain of the op-amp is finite, node B in Fig. 3.7 is allowed to slightly change as the current in the DAC changes. The error caused by the finite op-amp gain effect is negligible as the INL is less than 0.06 LSB.

The final issue to investigate in the analysis of the output mirror circuit is op-amp offset. Figure 3.10 shows the output of the mirror circuit without any op-amp offset. Op-amp offset is quite difficult to predict since it depends solely on the matching of the devices inside the amplifier. Figure 3.11 shows the INL and DNL of an ideal current mirror when the op-amp in the output circuit has 10mV of offset. It can be seen from Fig. 3.11 that even with 10mV of op-amp offset the INL is less than 0.9 LSB. More importantly, Fig. 3.11 shows the negligible effect that op-amp
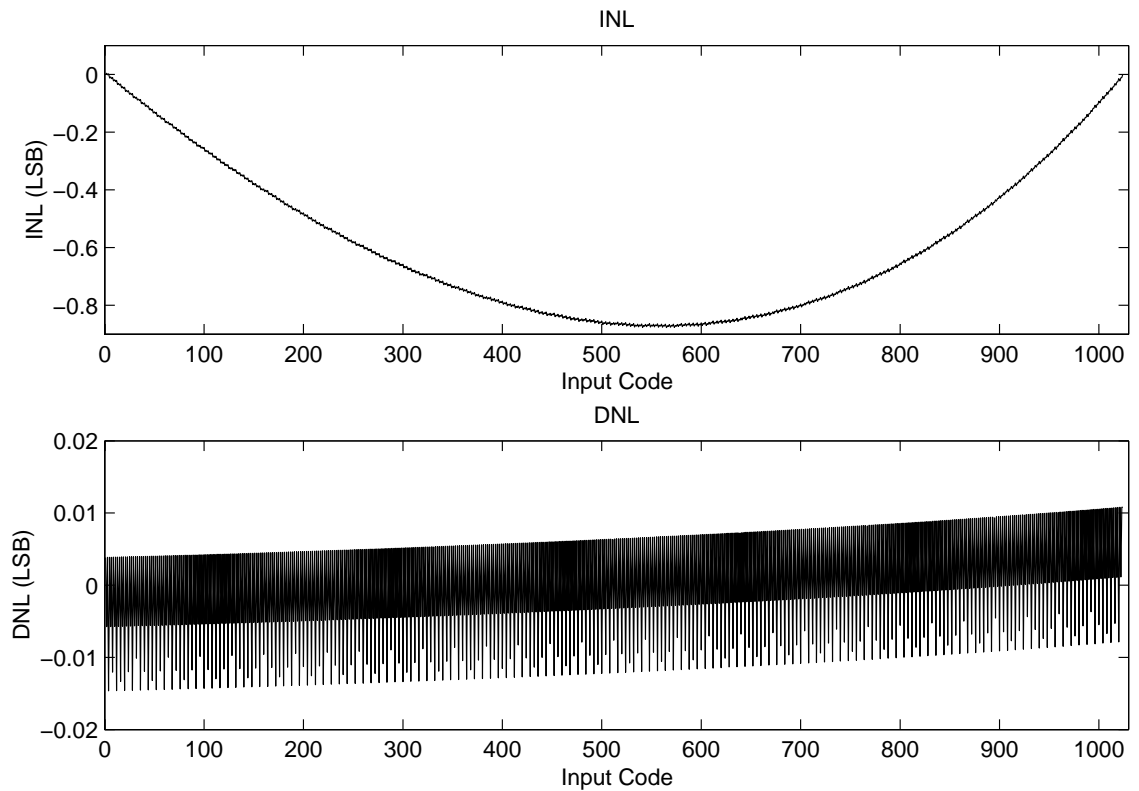
FIGURE 3.12: INL and DNL for Actual Mirrored Output With 10mV Offset.

offset has on DNL. Figure 3.12 shows the actual INL and DNL at the output of the current mirror when 10mV of op-amp offset is introduced. Figure 3.12 clearly shows that the actual response of Fig. 3.10 with no offset present is directly mapped onto the ideal response of Fig. 3.11. Just as in the ideal case, Fig. 3.12 shows a negligible effect on the DNL, while the INL still performs within the required 10-Bit range.

4.   ULTRA HIGH GAIN OP-AMP DESIGN

Operational amplifiers (op-amps) are one of the key building blocks in today's mixed-signal area. Extensive research has been done in the op-amp area to achieve all sorts of different results. Research of general purpose op-amps is slowly becoming a thing of the past, where now op-amps are often designed with a specific application in mind. Some applications require op-amps with extremely high bandwidth, while others may require ultra high gain, low noise, low DC offset, fast settling time, or just about any combination of these parameters. This chapter introduces a few basic op-amp architectures as well as the basic figures of merit used in the design process. The novel feed-forward architecture and extensive MATLAB modeling of the implemented op-amp are presented. Design considerations for the low voltage operation of the op-amp will be briefly discussed before the results of SPICE simulations are presented. Just as in the case of the DAC design, extensive use of the 0.18 μm CMOS process specifications are used to ensure op-amp performance over the wide range of temperature and process variations.

4.1   Op-Amp Basics

Figure 4.1 shows simplified schematics of the two most common op-amp architectures. The gain of a single stage is simply the transconductance (gm) of the input transistor multiplied by the impedance seen at the output node (R_{out}), therefore gain is $\frac{Vout}{Vin} = gm_{in} \times R_{out}$. The cascaded op-amp uses a chain of simple gain stages to achieve higher gain at the output. Since the gain of the first stage is multiplied by the gain of the second stage, the total output gain is $\frac{Vout}{Vin} = gm_1 r_{o1} * gm_2 r_{o2}$. The cascode op-amp of Fig. 4.1 uses a stacking method to create a higher output
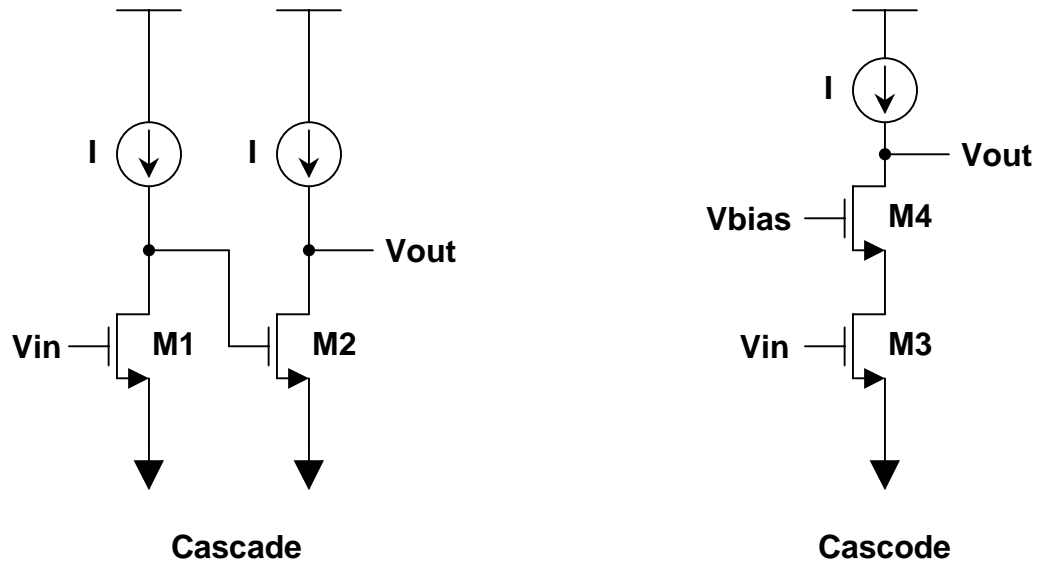
FIGURE 4.1: Simplified Cascade and Cascode Amplifiers.

impedance than a single stage. The impedance seen at the output is $gm_4 r_{o4} r_{o3}$, and if r_{o3} and r_{o4} are equal, then the output impedance is $gm_4 r_o^2$. If gm_3 equals gm_4, then the gain of the cascode op-amp is $\frac{Vout}{Vin} = gm^2 r_o^2$, which is almost exactly the same as the gain for the cascade stage. Both architectures have their advantages and drawbacks that can be better understood after reviewing a few basic figures of merit.

The figures of merit most commonly referred to for op-amps are gain, bandwidth (BW), phase margin (PM), and DC offset. Figure 4.2 shows the response of a basic two pole system. DC gain is often quoted in dB as shown in the figure, and represents the output voltage divided by the input voltage at low frequencies. The bandwidth of an amplifier can either be expressed as 3 dB BW where the gain falls 3 dB lower than its low frequency value, or as unity gain bandwidth (UGBW) where the amplifier has a gain of 1 (0dB). UGBW is the common reference when one speaks of BW, but this is not always the rule. The phase margin represents the
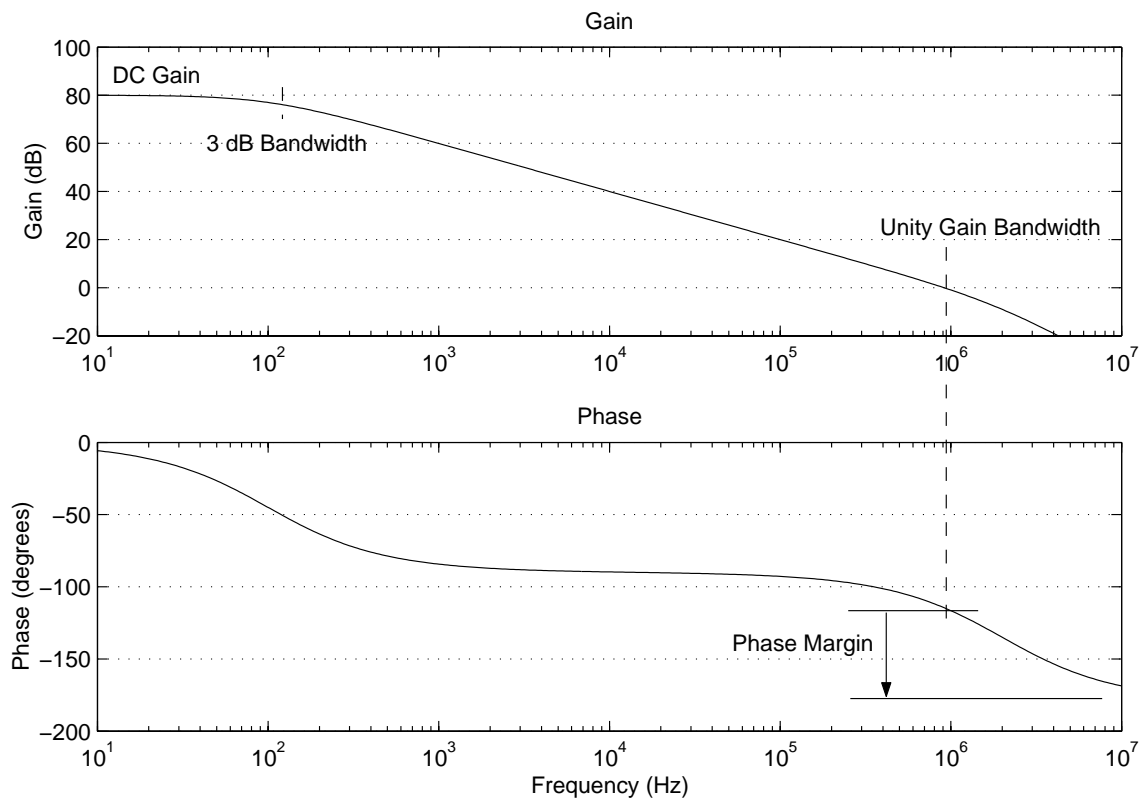
FIGURE 4.2: Gain and Phase Response For 2 Pole System.

difference between the phase of the output signal and $-180°$. The phase margin is usually the greatest indicator of op-amp stability. When the phase margin is high (eg. phase of output is $-100°$), the settling time behavior of the op-amp will be good because the op-amp is very stable. As the phase of the output signal gets close to $-180°$, the op-amp approaches an unstable condition where the output will oscillate.

Figure 4.3 shows the settling behavior of a basic two pole op-amp in unity gain configuration with a phase margin of $70°$ when a 1 V step is applied to the input. Figure 4.4 shows the settling behavior of the same circuit, but with only $20°$ of phase margin. The ringing behavior seen in Fig. 4.4 is a good indicator that the op-amp is near the unstable condition. If the phase margin had been closer to zero, the output response would show a continuous oscillation, with little to no damping. DC offset is the difference between the voltages at the inputs of an op-amp when connected in the unity gain configuration. If the non-inverting input is set to 1V, and the output (inverting input) has a voltage of 1.010V, then the op-amp offset is 10mV. Op-amp offset has negative effects in almost all applications, and is often eliminated by calibration in the continuous time or cancelled with capacitors in a sampled-data system.

4.2   Architecture Design

The application for an op-amp that presents itself repeatedly in the DAC design is servoing. In order to have an accurate servo, the op-amp which acts as the servoing device needs to have a very high DC gain. As discussed briefly in section 4.1, both the cascade and cascode op-amps of Fig. 4.1 allow for high DC gain. The primary problem associated with the cascode op-amp is a lack of headroom. Since the DAC and op-amp can only operate from a 1.8V power supply, limitations
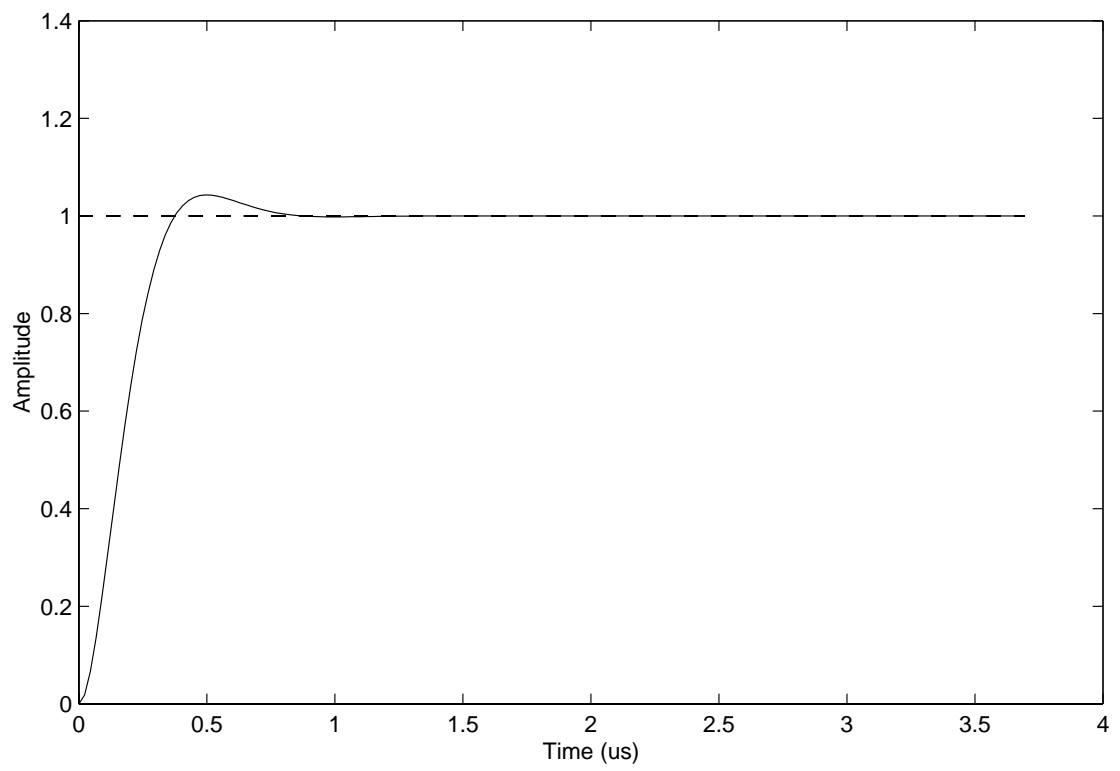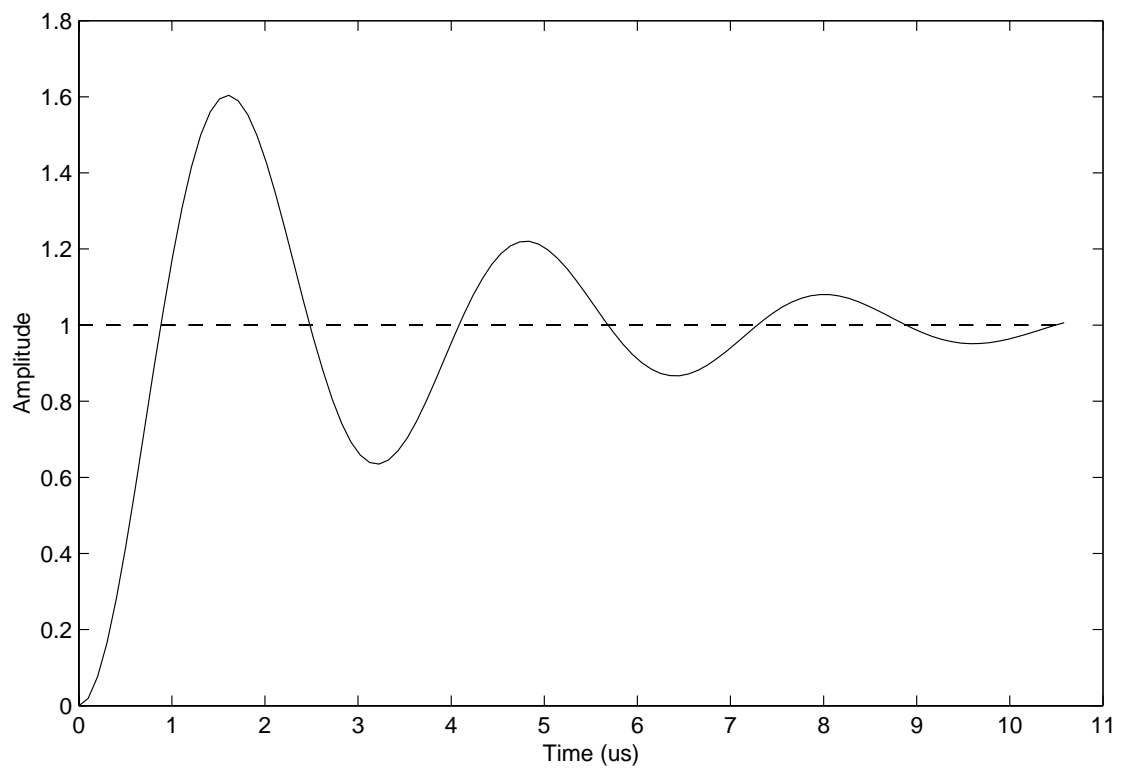
FIGURE 4.3: Unit Step Response When $PM = 70°$.

FIGURE 4.4: Unit Step Response When $PM = 20°$.

are quickly introduced for the cascode design. The amount of drain-source voltage available for each transistor in a cascode design with a 1.8V power supply is quite limited. This limited drain-source voltage upon biasing implies that the output voltage is not allowed to change very much without either the upper or lower (M3, M4, Fig. 4.1) devices entering the triode region. In order to maintain high output impedance, and hence high gain, the devices are not allowed to enter the triode region at any point of operation.

Since the low voltage power supply limits the use of cascoding in this design, a cascaded architecture is chosen. The primary problem associated with cascading op-amps is the phase of the output signal. Figure 4.5 shows a cascade of 4 ideal op-amps. Each op-amp represented by the ideal block is considered a single pole system, which means that each stage introduces $90°$ of phase lag. If each stage adds $90°$ of phase lag, then the output signal will have a phase of $-360°$. As mentioned in section 4.1, an output signal with phase less than $-180°$ will be unstable, and therefore useless as an op-amp.

The architecture chosen to eliminate the problems associated with the stability of a cascaded system is feed-forward compensation. This method of compensation, shown in Fig. 4.6, allows the input signal to travel through the path composed of A_1-A_4 at low frequencies, while high frequency inputs travel through the path composed of A_1 and A_{ff}. Therefore, the op-amp performs as a 4 stage cascaded op-amp at low frequencies to achieve ultra high DC gain, and as a 2 stage op-amp at high frequencies to allow for a sufficient phase margin at the UGBW. Figure 4.6
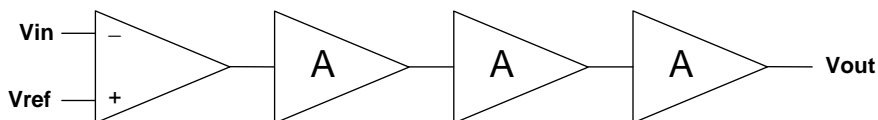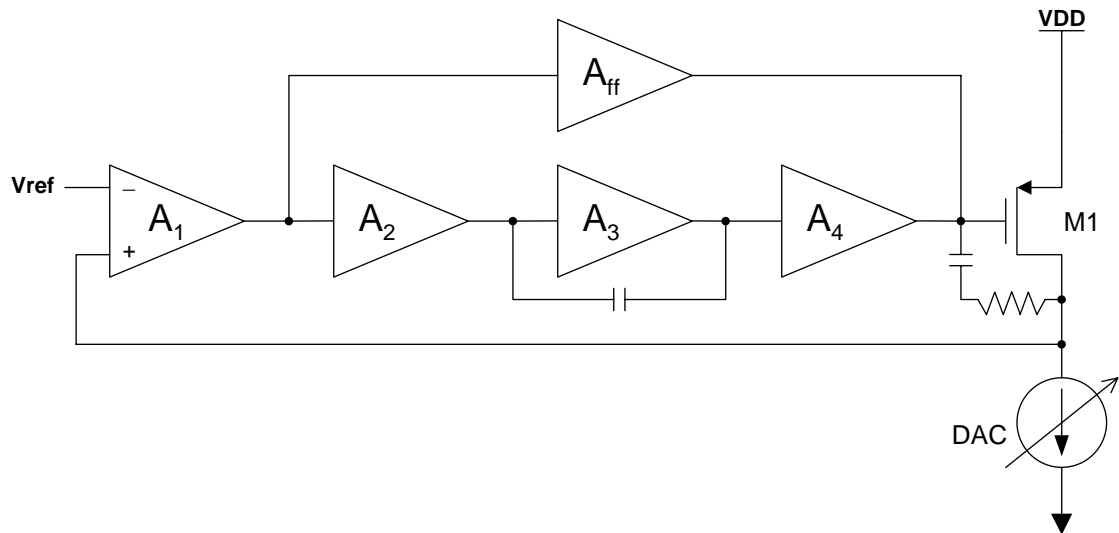

FIGURE 4.5: Cascade of Ideal Op-Amps.

FIGURE 4.6: Feed-Forward Amplifier With Feedback.

shows the closed loop servoing operation of the op-amp. The device being servoed (M1) acts as a gain stage in the feedback loop, and therefore must be included in the simulation of the amplifier. The design must be performed such that there is sufficient phase margin around the loop, therefore M1 is included in the op-amp schematics and simulations, even though it is not technically a part of the op-amp.

4.3 MATLAB Modeling of Feed-Forward Compensation

The relationship between phase margin and settling time was introduced in section 4.1 for a two pole system. The relationship for the two pole system is widely used and well understood. The basic relationship between phase margin and settling time does not always hold for the case of the feed-forward op-amp of Fig. 4.6. The main reason that the relationship does not directly carry over for the feed-forward amplifier is because of the zeros introduced in the transfer function by the feed-forward device. The amplifier of Fig. 4.5 has four poles and no zeros. The amplifier

of Fig. 4.6 has six poles and three zeros around the loop. Each op-amp has a pole, plus one pole from the feedback device (M1), for a total of six. The three zeros arise from the feed-forward stage that bypasses three op-amps.

In order to better understand and predict what the op-amp response will look like when simulated in SPICE, a first order MATLAB model was developed. This model allows the designer to view the pole and zero locations, and observe how changing parameters in the design effects the overall transfer function. Figure 4.7 shows the small signal model used to derive the equations for the MATLAB model. Figure 4.8 shows the actual op-amp schematic. The labeling of the small signal model in Fig. 4.7 is consistent with the actual op-amp of Fig. 4.8. The transfer function from Vin to $V1$ is:

$$\frac{gm_1 R_1}{(1 + sR_{1b}C_{1b})}$$

The calculated transfer function from $V1$ to $V3$ is:

$$\frac{gm_2 gm_3 R_2 R_3 (1 - \frac{sC_1}{gm_3} + sR_1 C_1)}{cs^3 + bs^2 + as + 1}$$

where:

$$
\begin{aligned}
c &= R_1 R_2 R_3 C_1 C_2 C_3 \\
b &= R_2 R_3 (C_1 C_2 + C_1 C_3 + C_2 C_3) + R_1 C_1 (R_2 C_2 + R_3 C_3) \\
a &= R_2 (C_1 + C_2) + R_3 (C_1 + C_3) + gm_3 R_2 R_3 C_1 + R_1 C_1
\end{aligned}
$$
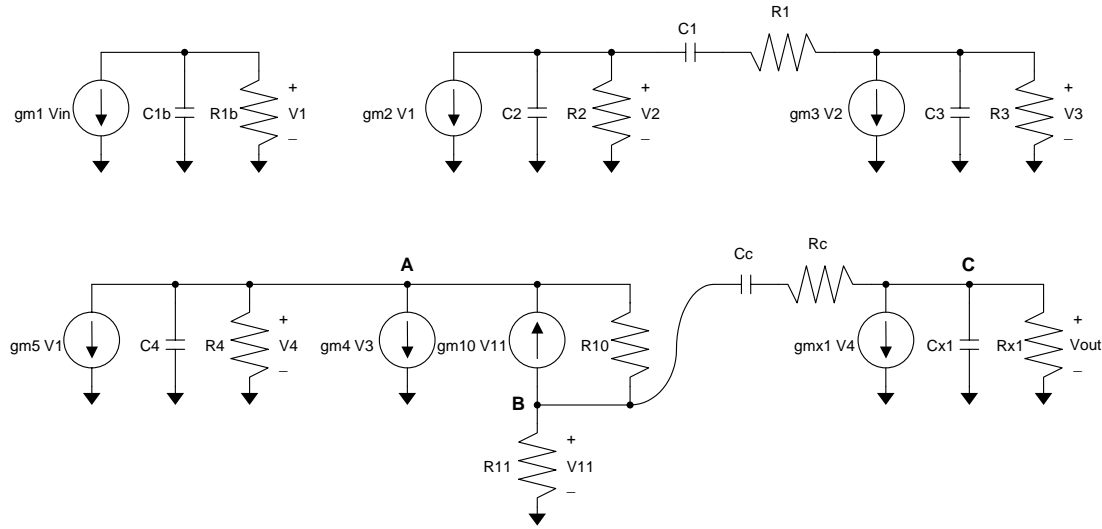
FIGURE 4.7: Small Signal Model Used to Create Mathematical Model.

Node equations can be written at **A**, **B**, and **C** as:

$$\mathbf{A} \quad : \quad gm_5V_1 + \frac{V_4}{Z_4} + gm_4V_3 - gm_{10}V_{11} + \frac{V_4 - V_{11}}{R_{10}} = 0$$

$$\mathbf{B} \quad : \quad \frac{V_{11}}{R_{11}} + \frac{V_{11} - V_4}{R_{10}} + gm_{10}V_{11} + \frac{V_{11} - V_{out}}{Z_C} = 0$$

$$\mathbf{C} \quad : \quad \frac{V_{out}}{Z_{X1}} + gm_{X1}V_4 + \frac{V_{out} - V_{11}}{Z_C} = 0$$

The final transfer function for the whole system, $H = \frac{Vout}{Vin}$, ends up with a 4th order numerator and an 7th order denominator. The coefficients of the resulting transfer function are too numerous to list, but Fig. 4.10 shows the resulting amplifier response. Figure 4.10 shows that the MATLAB model predicts a DC gain of 130dB and a phase margin of 100°. The figure shows that the phase begins to droop and head toward an unstable amplifier condition before it climbs back into the region of desirable phase margin. The shape of the curves can be explained from the
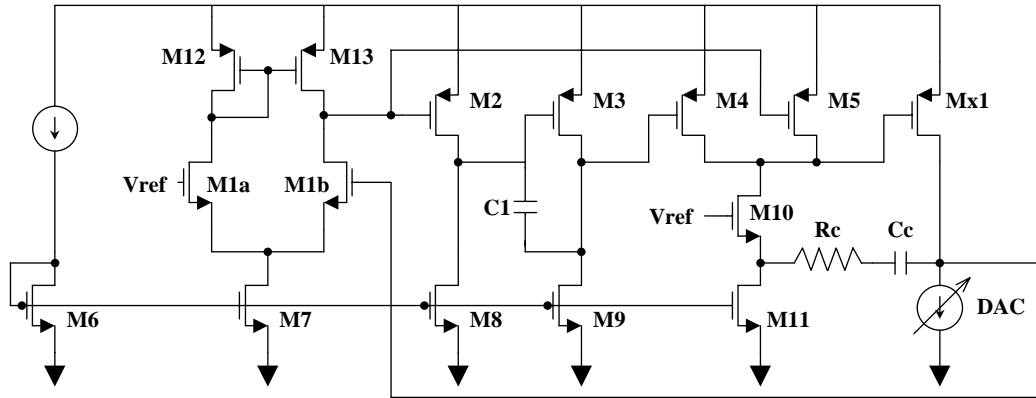
FIGURE 4.8: Feed-Forward Amplifier Schematic.

pole/zero plot of Fig. 4.9. Figure 4.9 shows that as the frequency increases, the signal originally sees two poles before the zeros begin to enter and correct the phase of the transfer function. The right-half-plane zero that would normally be present because of the miller capacitor C1 is moved to the left half plane due to a larger left-half-plane zero created by the feed-forward stage.

Figure 4.9 also shows a zoomed in view of a pole/zero doublet. This doublet is created as a zero from the feed-forward device is placed very close to one of the poles from the low frequency stages. It is unclear exactly how the presence of the pole/zero doublet effects the settling time [24, 25], but it is known that the presence of a pole/zero doublet does degrade the settling time. SPICE simulations show that the op-amp still settles to within 0.01% in 25 ns, making it more than adequate for the DC application.

4.4 Simulation Results

The amplifier design of Fig. 4.8 was designed and simulated using SPICE after making initial parameter settings with the MATLAB model. As was previ-
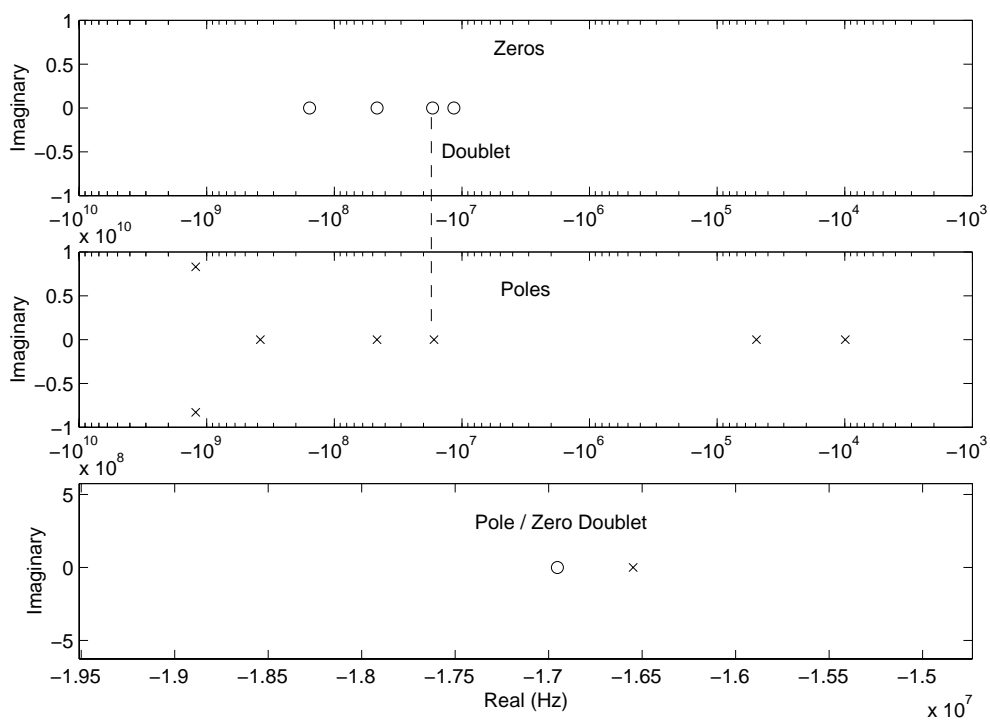
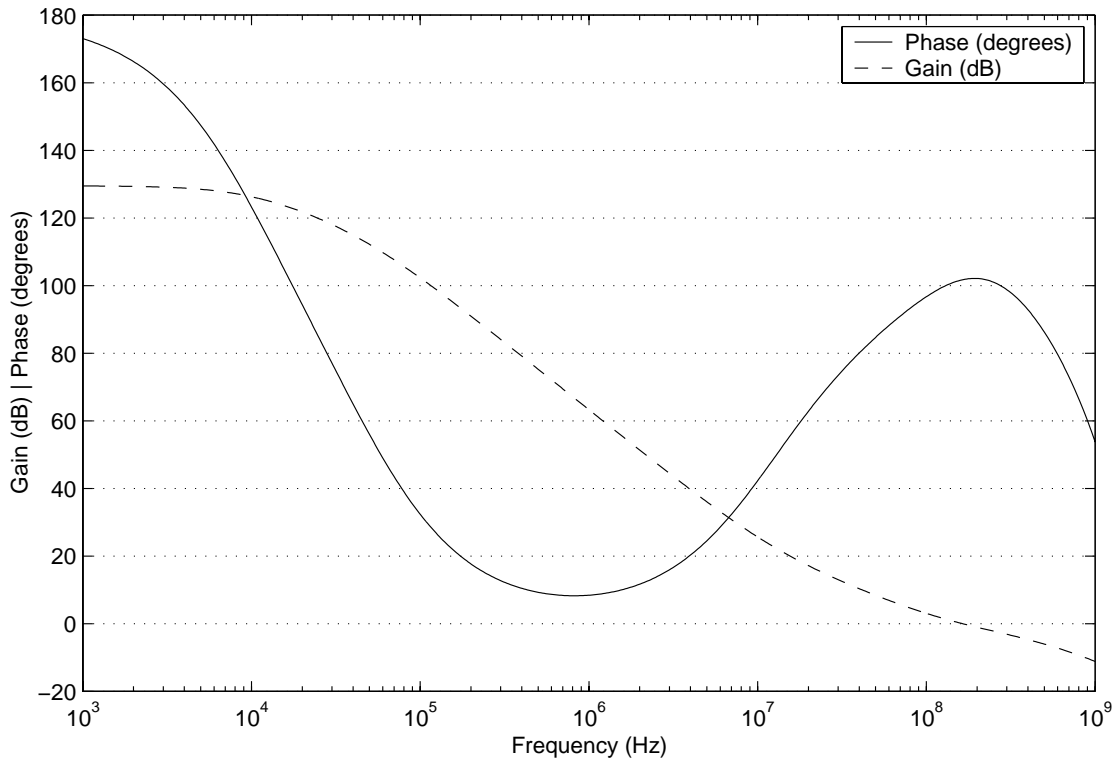FIGURE 4.9: Predicted Pole/Zero Locations.
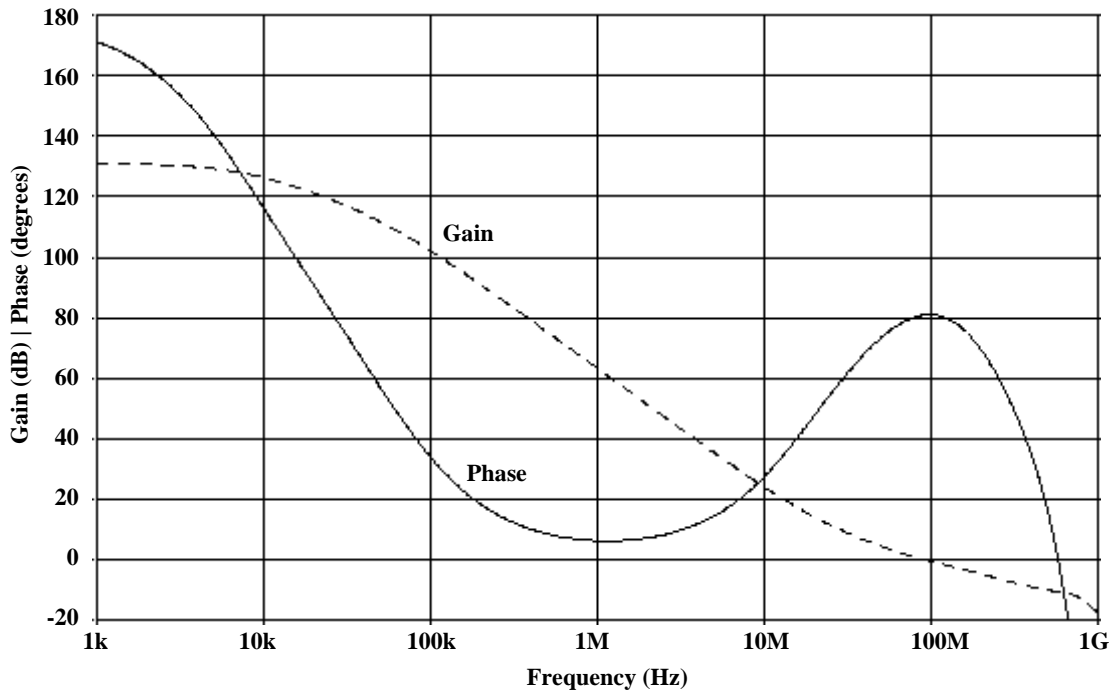
FIGURE 4.10: Predicted Amplifier Response.

FIGURE 4.11: Actual Simulated Amplifier Response.

ously mentioned, the amplifier was simulated for loop characteristics, and therefore Fig. 4.8 shows the feed-back device Mx1 in the schematic. Figure 4.11 shows the actual loop response when simulated in SPICE. The DC gain exactly matches the MATLAB model prediction of Fig. 4.10. Both of the curves (gain and phase) match the predicted response of Fig. 4.10 extremely well. One anticipated difference is the phase response above 20 MHz. The model predicted 100° phase margin, while the actual simulations show that the phase margin is really 80°. The 100° prediction made by the model only accounts for first order poles in the system and does not correctly model the higher order poles which create the actual phase response seen in Fig. 4.11.

5. IMPLEMENTATION

Considering the process and temperature variations of the device parameters, a 10-Bit DAC was designed and implemented in TSMC's digital 0.18 μm CMOS process. This process has a single-poly layer and 5 metal layers. The fabricated chip was packaged in a 52-pin PLCC package. The design was simulated in SPICE and modeled effectively in MATLAB before fabrication. Extensive area optimization was done to minimize the die space required for the layout. Recall that Fig. 3.2 shows the schematic of the final DAC core. The implemented chip includes all the digital circuitry and the linear output circuit discussed earlier.

The chip layout is shown in Fig. 5.1. The center of the layout is occupied by the array of current source devices. The four servoing op-amps are at the top of the figure, while the resistor array runs vertically along the right side. The left side of Fig. 5.1 shows the input latches and decoding logic followed by the metal routing to the switches, and finally the switches directly to the left of the current source array. The DAC measures 110 μm $\times$ 94 μm, which consumes only 0.0104 mm^2 of area.

The op-amps shown in Fig. 5.1 are a slight variation from the op-amp described in chapter 4. Simulations have shown that op-amp DC gain in excess of 80dB does not further improve the performance of the DAC. For this reason, the op-amp from chapter 4 was optimized to consume less area, and therefore the number of stages was decreased from four to two. Utilizing a two stage op-amp requires only one capacitor and allows the area to be small enough to place four op-amps above the DAC core as shown in Fig. 5.1.

This chapter describes the measurement setup in detail, including the design of the test board. The measurements presented at the end of this chapter are in strong agreement with the simulation results presented in chapter 3.
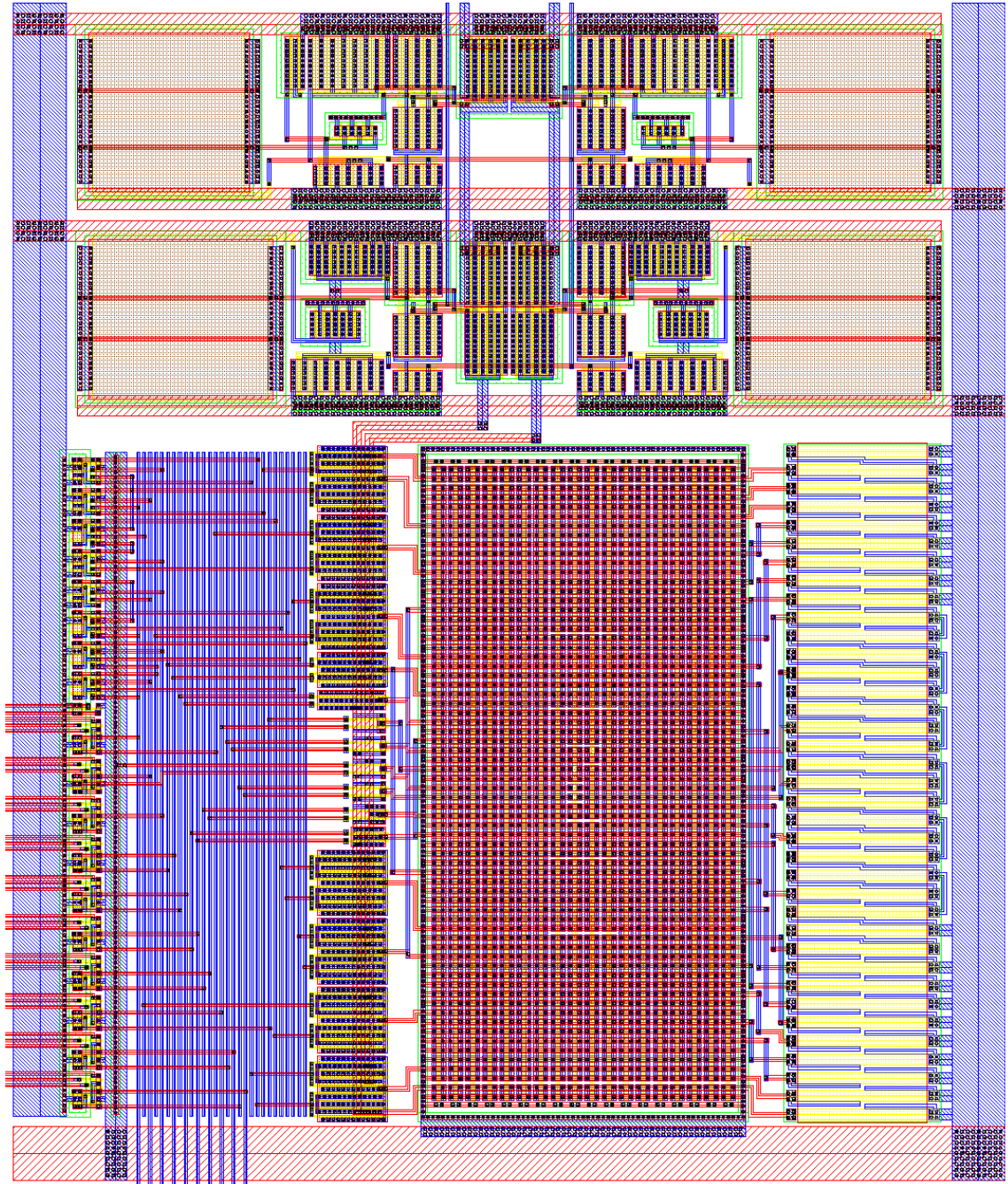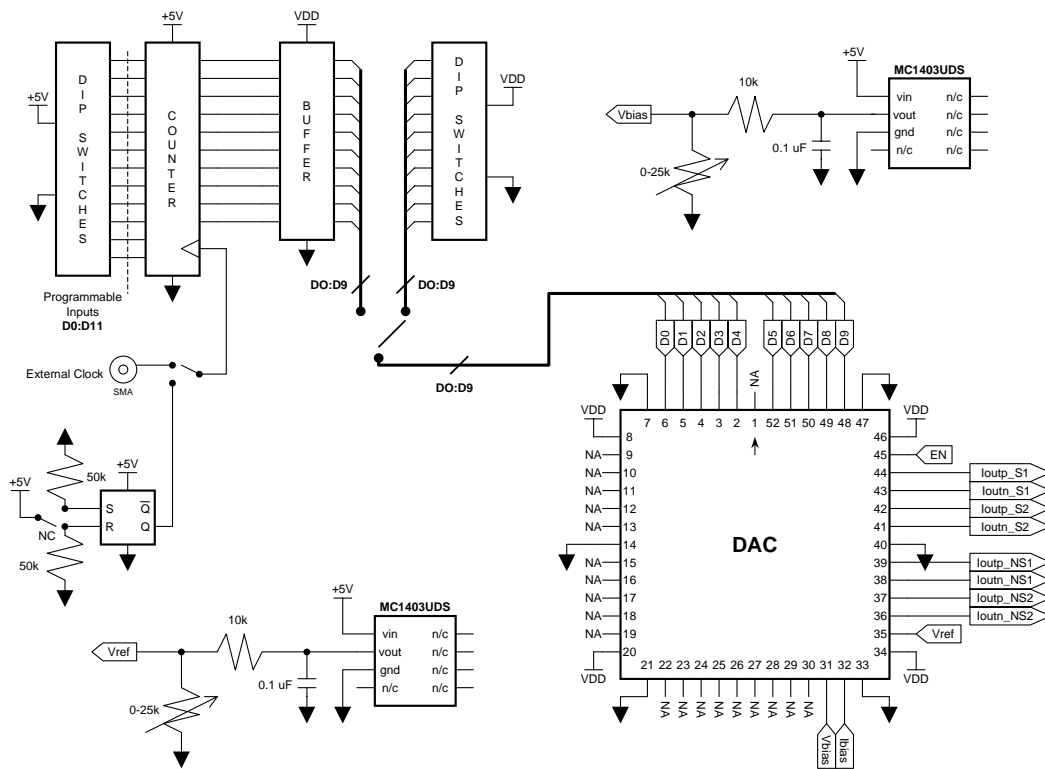
FIGURE 5.1: 10-Bit DAC Layout.

FIGURE 5.2: DAC Test Board.

5.1 Measurement Setup

In order to measure the performance of the DAC with accuracy and repeatability, a test board was designed and fabricated for testing the chip. A functional diagram of the test board is shown in Fig. 5.2. Figure 5.2 shows that the input to the DAC can either be controlled manually by selecting the appropriate code with a set of DIP switches or by a binary counter. The binary counter advances to the next binary code with every clock pulse that it receives. This clock can be manually controlled with a switch, or driven externally from an outside source. Figure 5.2 also shows some precision voltage reference chips used to develop the needed bias voltages and current.
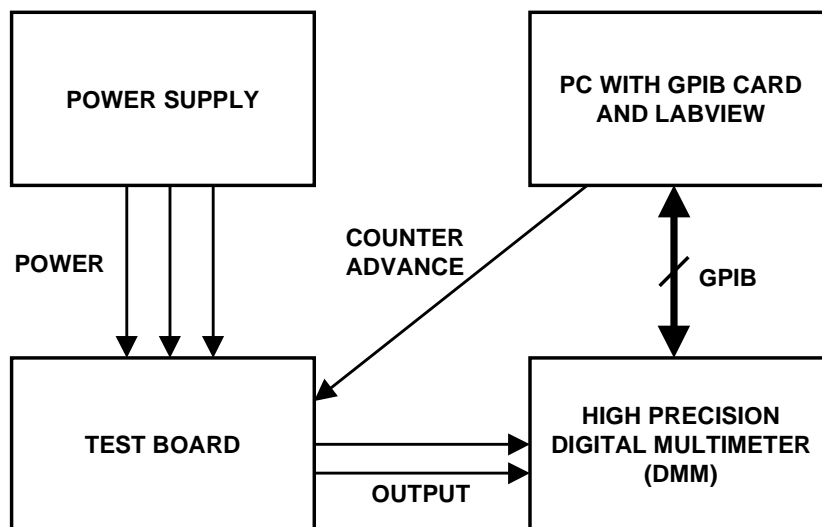
FIGURE 5.3: DAC Measurement Setup.

The measurement setup has been automated with the help of LabView and the appropriate GPIB test equipment. Figure 5.3 shows a functional diagram of the measurement setup. The figure shows a high precision DMM connected to the output of the DAC to measure the analog voltages at the output. This DMM is connected to a PC via a GPIB interface. The GPIB interface allows the computer to capture all the data from the DMM and store it in a file, or make mathematical calculations on the data. LabView is the software program used on the PC to interface with the DMM and capture the data. A single pin on the parallel port of the PC is used to advance the binary counter to the next code once all the data for a particular code has been captured. This process repeats itself until all 1024 input codes have been tested. The automated testing allows for easy and reliable testing over the entire lot of sample chips.

5.2   Experimental Results

Measurements were taken on ten different DACs provided upon fabrication. Using the measurement setup described earlier, LabView was used to capture 100 analog output data points for every input code. These data points were averaged for each input code, resulting in only one analog output per input code. Figure 5.4 shows the analog output as a function of input code. The data used to create Fig. 5.4 was measured using the differential output of the DAC. Figure 5.5 shows the best case measured INL and DNL for the 10-Bit DAC with the linear output current mirror described in chapter 3. Figure 5.5 shows that the INL is nearly 1 LSB peak-peak which means that this DAC is almost truly 10-Bit linear. The DNL plot of Fig. 5.5 shows that the DAC is 10-Bit monotonic.

The fact that the DAC measures 10-Bit monotonicity is the most impressive statistic since the original goal was to achieve 10-Bit monotonicity regardless of the linearity. As was mentioned in chapter 2, the DAC is monotonic if the DNL is greater than -1 LSB. Figure 5.5 shows the minimum DNL for the best case DAC tested is -0.263 LSB which is much greater than the -1 LSB minimum needed to maintain monotonicity. Even the common error transition from input code 0111111111 to 1000000000 does not have a large DNL spike. This transition is commonly referred to as the MSB transition, and is a common location for DNL errors in segmented architectures. The reason for the error at this particular transition is due to the fact that it is the largest number of currents being turned off, with only one current being turned on in its place over the entire input code range. A good DNL at this transition requires that the MSB current source be 1 LSB greater than the sum of all the other current sources in the DAC. Since every current source has some random variation, it is very difficult to match the MSB current source to the sum of many current sources; each of which contain a certain amount of random variation.
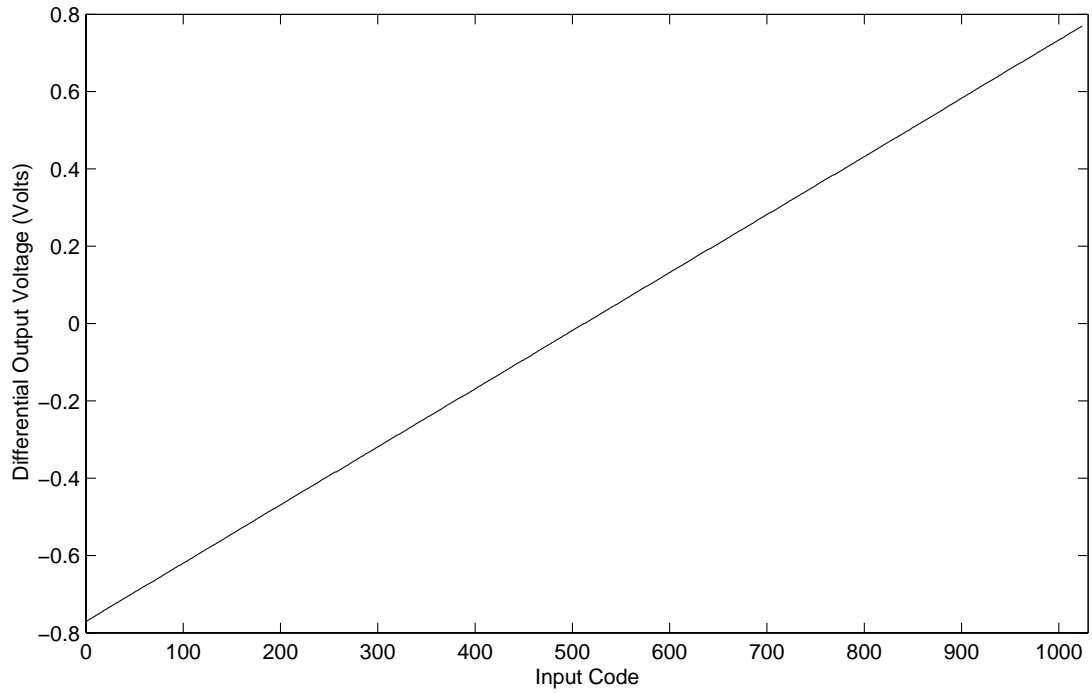
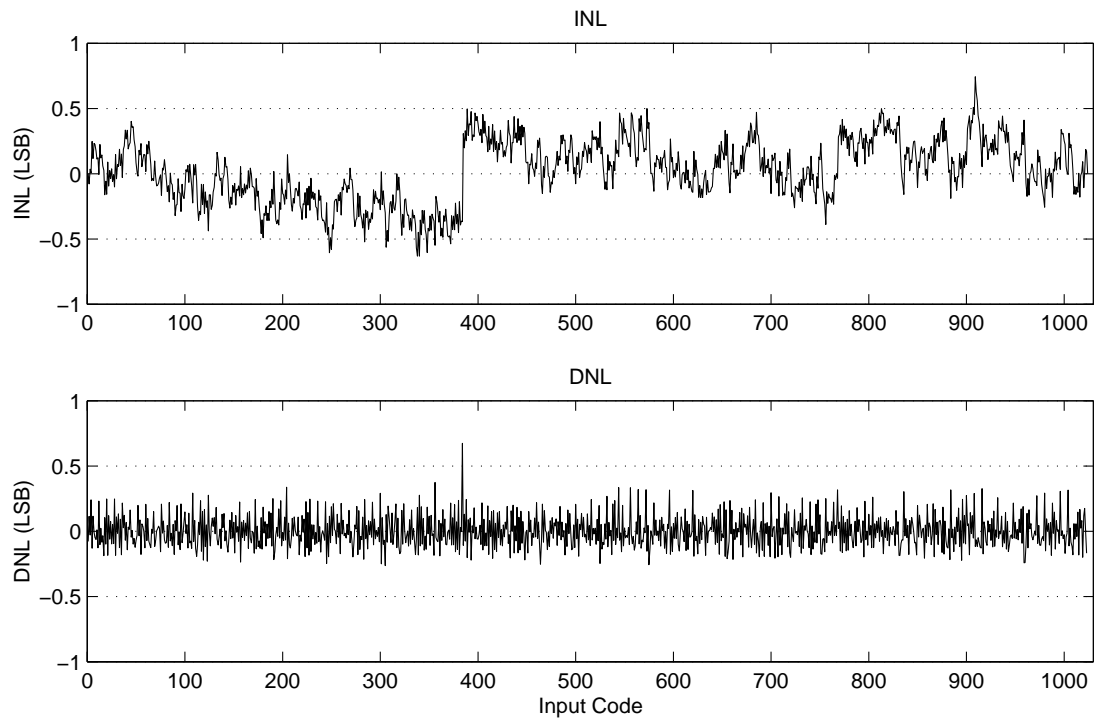FIGURE 5.4: Measured DAC Transfer Curve.

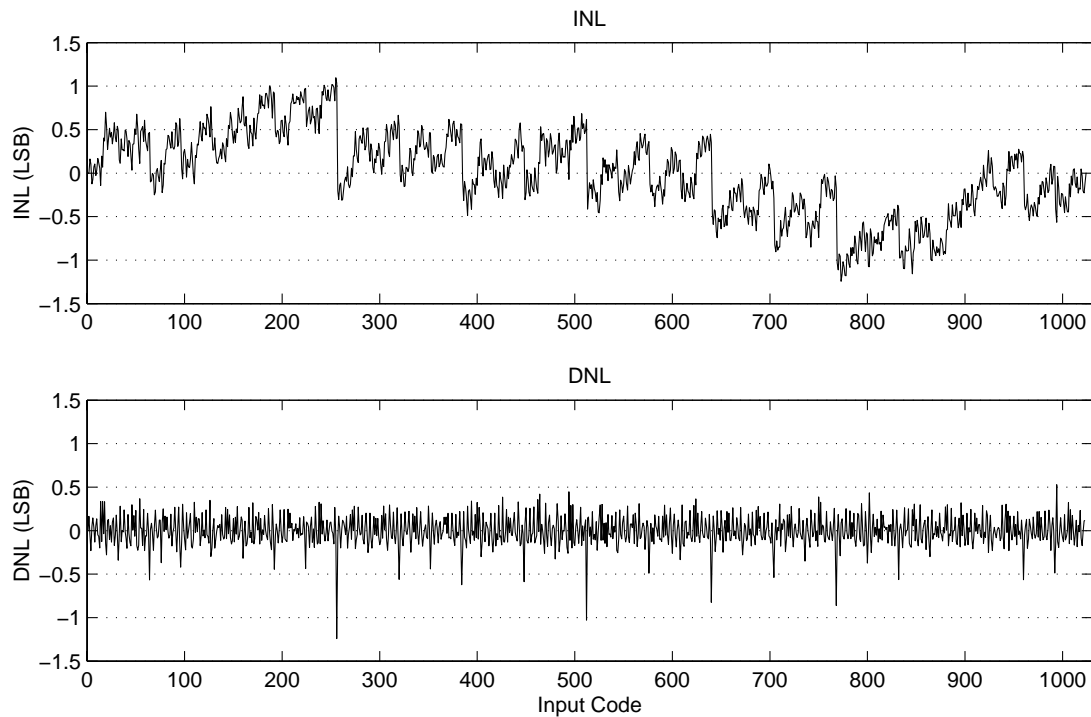FIGURE 5.5: Best Case Measured INL and DNL Performance.

FIGURE 5.6: Worst Case Measured INL and DNL Performance.

The monotonic condition was achieved on 8 out of the 10 tested DACs. In the 8 DACs where the monotonic condition was met, the linearity was better than 9-Bit linearity in all cases. Figure 5.6 shows the worst case performance of the 10 measured DACs. The DNL plot of Fig. 5.6 shows that the minimum DNL is -1.24 LSB, which is not sufficient for meeting the 10-Bit monotonic condition. The INL plot however shows that even with the non-ideal DNL performance, the DAC is still almost 9-Bit linear.

6. HIGHER RESOLUTION DAC DESIGN

While the 10-Bit DAC described in chapter 3 is suitable for most DC applications, there are instances where a DC DAC with a higher resolution than 10-Bits is required. Just as with the 10-Bit case, area consumption is of prime concern in this higher order DAC design. This chapter introduces a 13-Bit DC DAC design that utilizes the already high-accuracy 10-Bit core for minimal area consumption. The DAC architecture adds a minimal number of devices around the existing 10-Bit DAC to guarantee a monotonic behavior. The optimization of die area that resulted in the chosen device sizes is discussed in detail. The analysis of op-amp offset and current source device mismatch using SPICE will be examined before the final simulation results are presented.

6.1 Architecture Design

One of the primary goals of designing this 13-Bit DAC was to utilize the performance and accuracy of the 10-Bit core in order to build a 13-Bit DAC that guarantees monotonicity. Figure 6.1 shows the architecture of the 13-Bit DAC. The existing devices associated with the 10-Bit DAC are shown with dashed lines, while the new circuitry is shown with solid lines. One immediate difference that can be seen in this design vs. the 10-Bit design is that the 10-Bit core is no longer connected to ground. The node which was previously grounded in the 10-Bit design is now labeled as V_{DAC}. The bottom of Fig. 6.1 shows a set of current sources where the currents are steered in 1 of 3 possible directions by the 3 switches above the current sources. Although they are not all shown in Fig. 6.1, there are a total of 2^N (8) current sources, where N is the number of extra bits added, which in this case is 3.
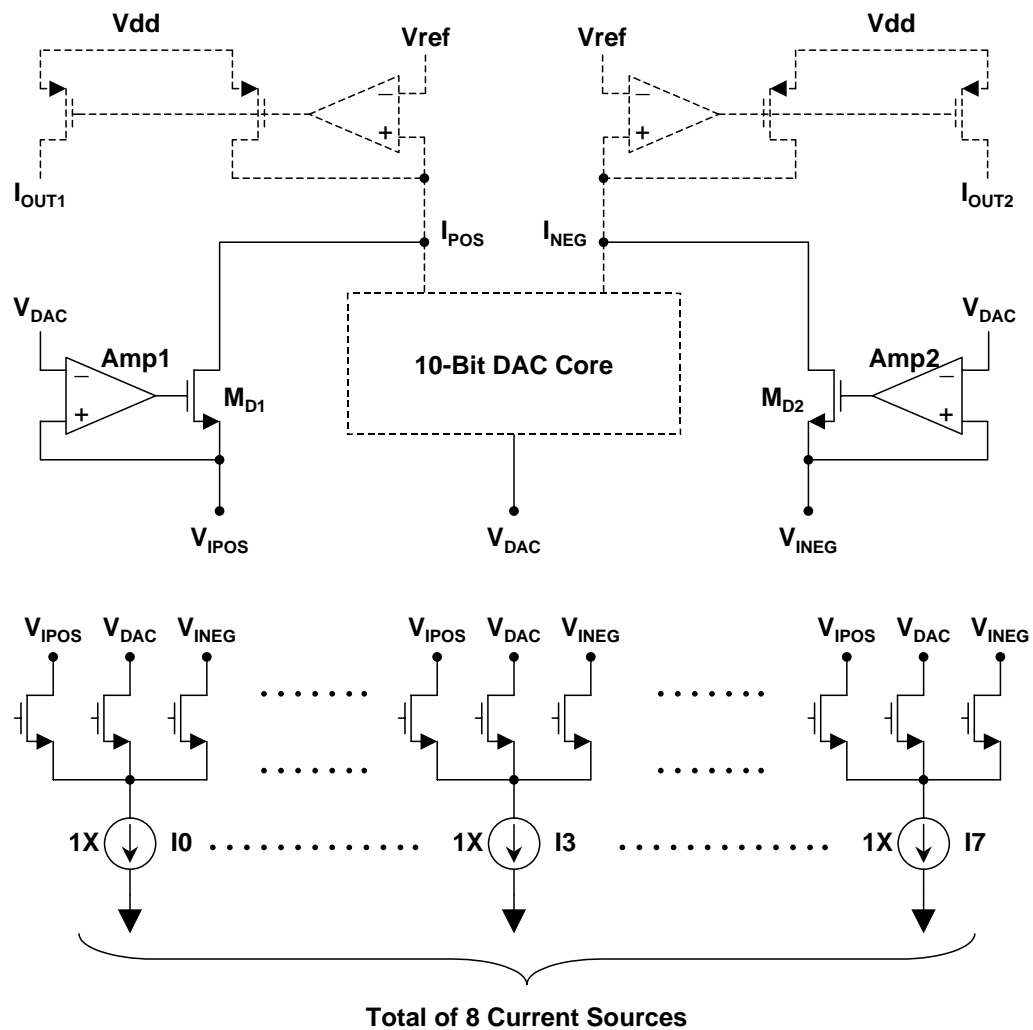
FIGURE 6.1: 13-Bit DAC Design.

The direction of each current is controlled by the switches above the current source. The switches are driven by a set of decoding logic which interprets the 3 extra MSBs of the binary input, and outputs control signals to the 24 different switches. In order to best describe the switching order of the current sources it is beneficial to investigate a few example conditions. Assume for the first condition that all the binary inputs (D0-D12) are low. In this condition, 7 of the current sources (I0-I6) will be connected to the V_{INEG} node. The remaining current source

I7 will be connected to the V_{DAC} node. There will be no connection to the V_{IPOS} node. The inside of the DAC core operates just as before, and in this case, will direct all of the I7 current through the I_{NEG} branch. For the second condition, assume that the input code has incremented to 0001111111111. At this point, the lower 8 current sources are in the same position as the first condition, but the DAC core is now directing all of the I7 current to the I_{POS} branch. When the code changes from 0001111111111 to 0010000000000, I7 is removed from the DAC core and connected to the V_{IPOS} node, while I6 is connected to the V_{DAC} node. This pattern repeats itself every 1024 (10-Bit) input codes as the input code increases. One by one, the current sources will be moved from the V_{INEG} node to the V_{DAC} node to the V_{IPOS} node. This method of operation will guarantee a monotonic behavior, assuming that the 10-Bit core is monotonic.

Besides the switching order of the lower current sources (I0-I6), there is another circuit design characteristic that ensures the monotonic behavior. The two dummy devices, M_{D1} and M_{D2}, are used in order to servo the V_{IPOS} and V_{INEG} nodes to the exact voltage below the DAC (V_{DAC}). Servoing so that all three of these voltages are the same ensures that any given current source (I0-I6) will generate the same current regardless of the node it is connected to. Ensuring the same current regardless of branch eliminates the possibility of any glitches in the transfer curve that could result in non-monotonicity.

6.2 Mismatch Modeling For Area Optimization

One problem associated with servoing M_{D1} and M_{D2} is op-amp offset. The DC offset of Amp1 and Amp2 will directly effect the voltage at V_{IPOS} and V_{INEG}. A difference in voltage at the three nodes will cause the currents to be slightly different as the current sources move from one node to the other. If this difference in current
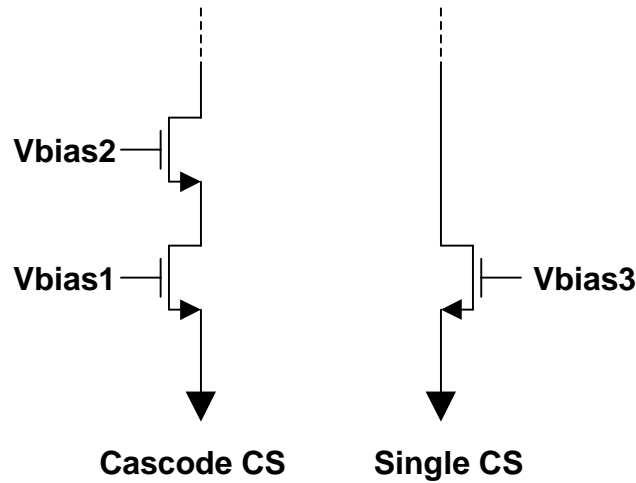
FIGURE 6.2: Single and Cascode Current Sources.

is larger than 1 LSB, then the system can become non-monotonic. In order to assure that a reasonable amount of op-amp offset can be tolerated, a mismatch analysis was performed in SPICE to choose the current source design.

SPICE simulations with 20 mV of op-amp offset quickly ruled out the use of a single device as a current source as shown on the right side of Fig. 6.2. The $\frac{W}{L}$ ratio needed to accommodate a 1 LSB change in current with a 20 mV change in drain voltage would have consumed a large amount of area. The cascode current source shown on the left of Fig. 6.2 however, has a much higher output impedance and is capable of tolerating a larger voltage swing at the drain of the top device with little change in current.

As shown in Fig. 6.3, there are switches between the top of the current source and the actual V_{IPOS}, V_{DAC}, and V_{INEG} nodes. These switches act as resistors with the size of the switches being inversely proportional to the resistance. As the $\frac{W}{L}$ ratio for the current source devices increases, the current source can tolerate a larger voltage swing for a fixed change in current. Therefore, as the size of the current source devices increases, the size of the switches decreases. Using 20 mV as the
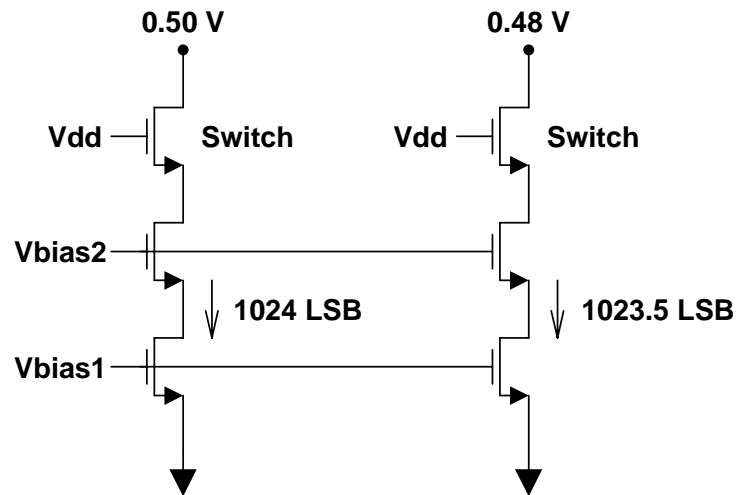
FIGURE 6.3: Cascode Current Sources With 20mV Offset Tolerance.

worst case op-amp offset, the current change tolerated is set to 0.5 LSB (Fig. 6.3), which is well under the 1 LSB change allowed to guarantee monotonicity.

SPICE simulations were performed for various switch and current source sizes with 20 mV offset corresponding to 0.5 LSB error in current. Figure 6.4 shows the minimum switch size allowed for various widths of the current source devices. It can be seen that the switch size decreases rapidly as the current source devices increase, but the trend is one of diminishing returns. In order to optimize the area consumed by these current sources and switches, the data from Fig. 6.4 was entered into MATLAB. Using the area equations determined by the design rules of the 0.18 μm process, Fig. 6.5 shows the area consumed by one cascode current source and three switches as a function of current source device size. Figure 6.5 shows that the optimum area consumption occurs when the current source devices have a width of 75 μm. The trend of Fig. 6.5 clearly shows that the switch size dominates the area when the current sources are small, but as the current sources become larger, the current source devices begin to dominate the area.
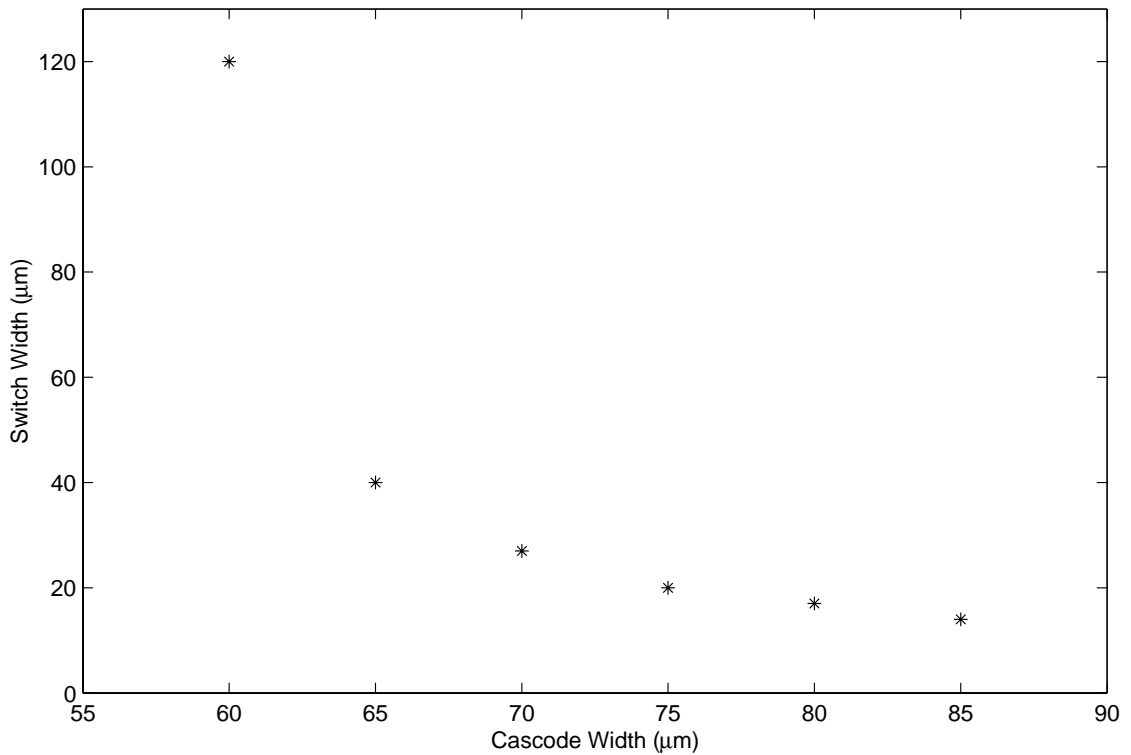
FIGURE 6.4: Switch Width vs. Current Source Device Width.

The remaining issue to investigate with mismatch modeling is the effect that mismatch between the current sources has on the overall transfer curve of the system. Figure 6.6 shows a hypothetical transfer curve for the 13-Bit DAC design with severely mismatched current sources. The markers along the piecewise linear curve break up the curve into sections corresponding to the 8 different current sources. In this example the mismatch was heavily over estimated for emphasis between the different segments of the curve. Despite the exaggeration of mismatch, Fig. 6.6 shows that even when the linearity of the system is compromised, the DAC remains fully monotonic.
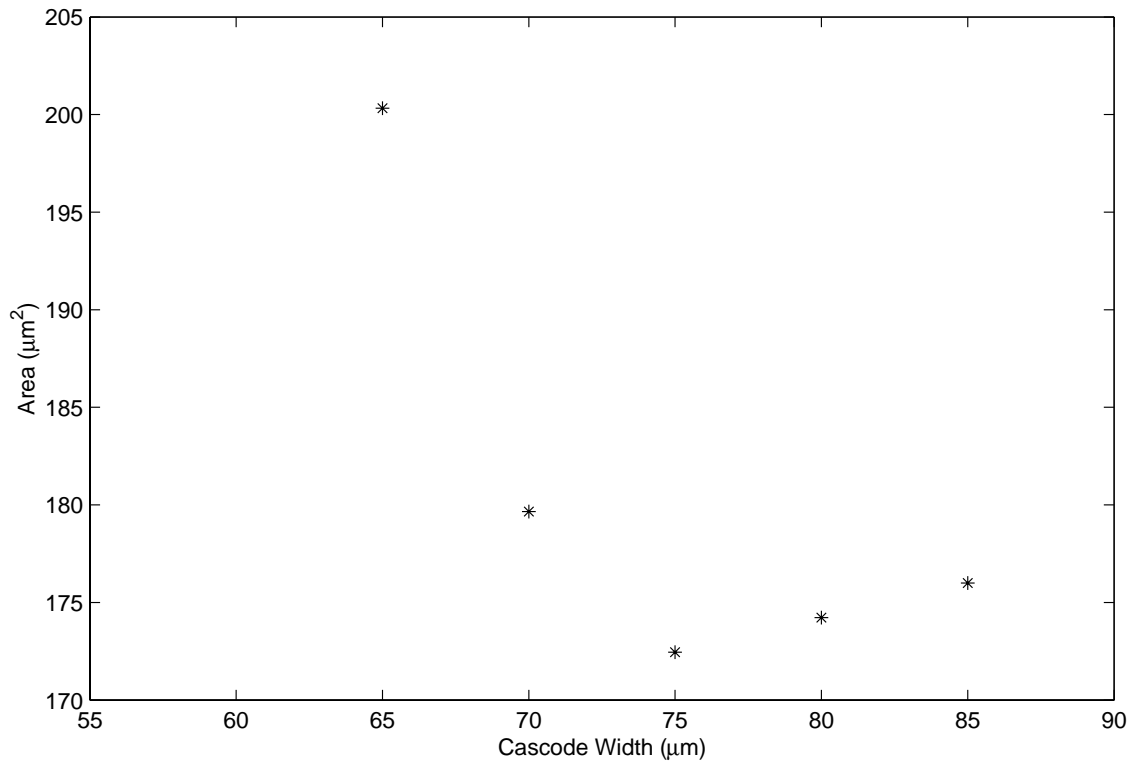
FIGURE 6.5: Area of CS and 3 Switches vs. CS Device Width.

6.3 Simulation Results

The final design consideration for the 13-Bit DAC reverts back to the design and simulation of the 10-Bit DAC of chapter 3. Recall that Fig. 3.2 shows a schematic of the implemented 10-Bit DAC core. As mentioned earlier, the bottom resistor string of the DAC core is no longer connected to ground in the 13-Bit design. In fact, SPICE simulations show that in order for the cascode current sources to operate as previously discussed, the voltage at V_{IPOS}, V_{DAC}, and V_{INEG} needs to be 500 mV. This increase in voltage below the resistor string directly relates to a decrease in the drain-source voltage available for the cascode devices in the core (M0-M13, Fig. 3.2).
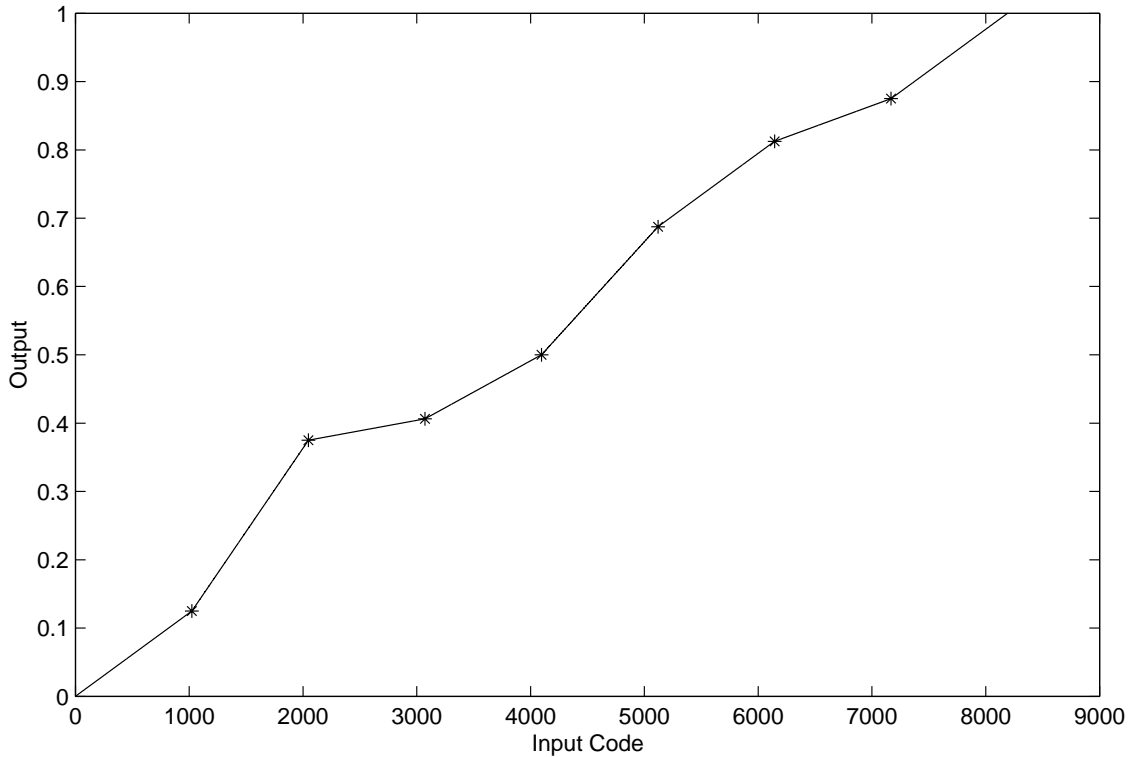
FIGURE 6.6: Transfer Curve for Severely Mismatched Current Sources.

Chapter 3 showed the effect of non-ideal switch sizing on the INL and DNL performance of the DAC. Now that the V_{DS} of the cascode devices (M0-M13, Fig. 3.2) is reduced by 500 mV, it is imperative to re-check the performance of the core. Figure 6.7 shows the INL of the DAC from chapter 3 and the INL for the DAC core used in the 13-Bit design with reduced headroom. Figure 6.8 shows the same comparison for DNL. It is clear by examining both figures that the changes in INL and DNL are negligible for the DAC core with reduced headroom.

This negligible change in INL and DNL performance can be explained with the simple IV curve of Fig. 6.9. Figure 6.9 shows the actual IV curve for the NMOS cascode devices in the DAC core (M0-M13, Fig. 3.2). Those devices have a length of 0.36 μm, and a width of 0.56 μm. The current for each device is 1.0 μA. Since the current is very low, these devices operate in the region shown in Fig. 6.9. In
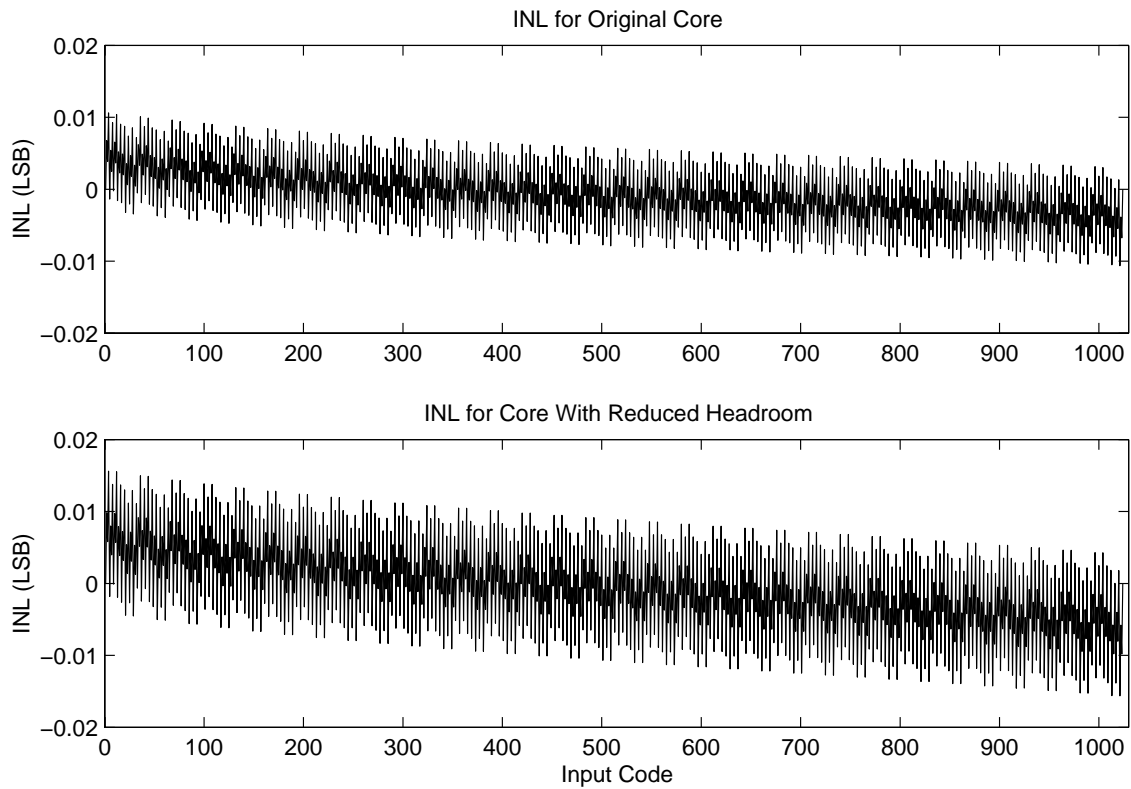
FIGURE 6.7: INL For Ch. 3 DAC and 13-Bit DAC Core.

the original DAC the cascode devices operate with 800 mV of V_{DS}, and in the 13-Bit design they are forced to operate at 300 mV V_{DS}. With the deep saturation operation shown in Fig. 6.9, the 500mV change in V_{DS} has such a small effect on the current that the INL and DNL remain almost zero in the 13-Bit DAC.

FIGURE 6.8: DNL For Ch. 3 DAC and 3-Bit DAC Core.

FIGURE 6.9: IV Curves For NMOS Cascode Inside DAC Core.

7. CONCLUSIONS

The key factor driving the design of the low voltage DC DACs presented in this thesis is area optimization and minimization. No previous CMOS DACs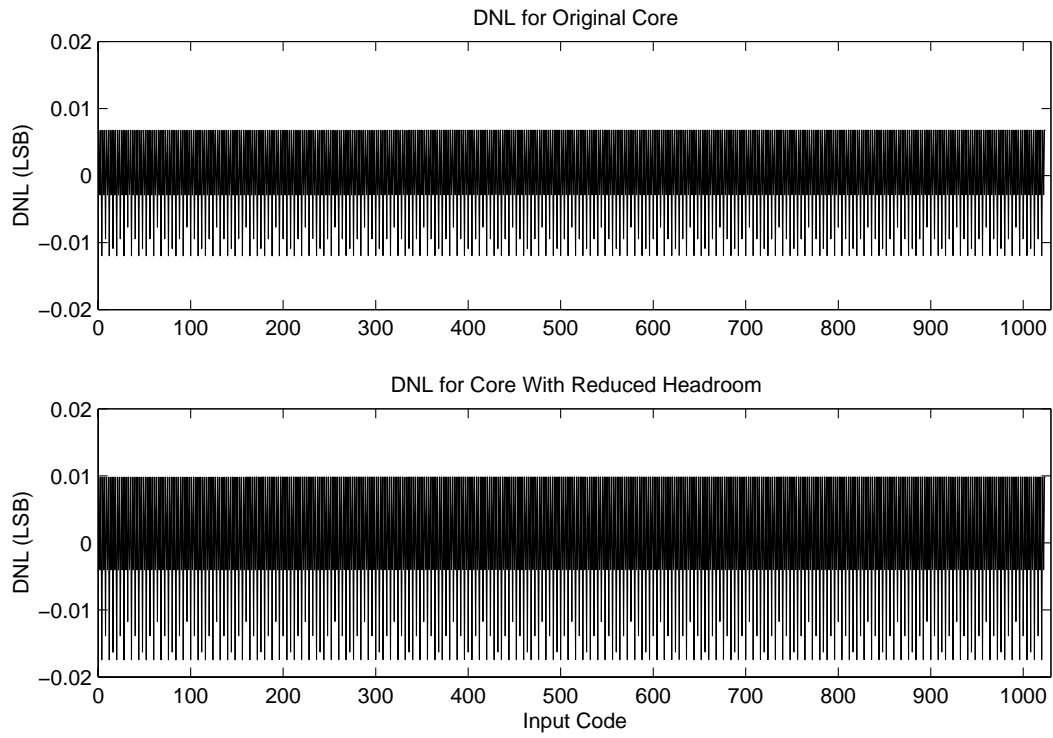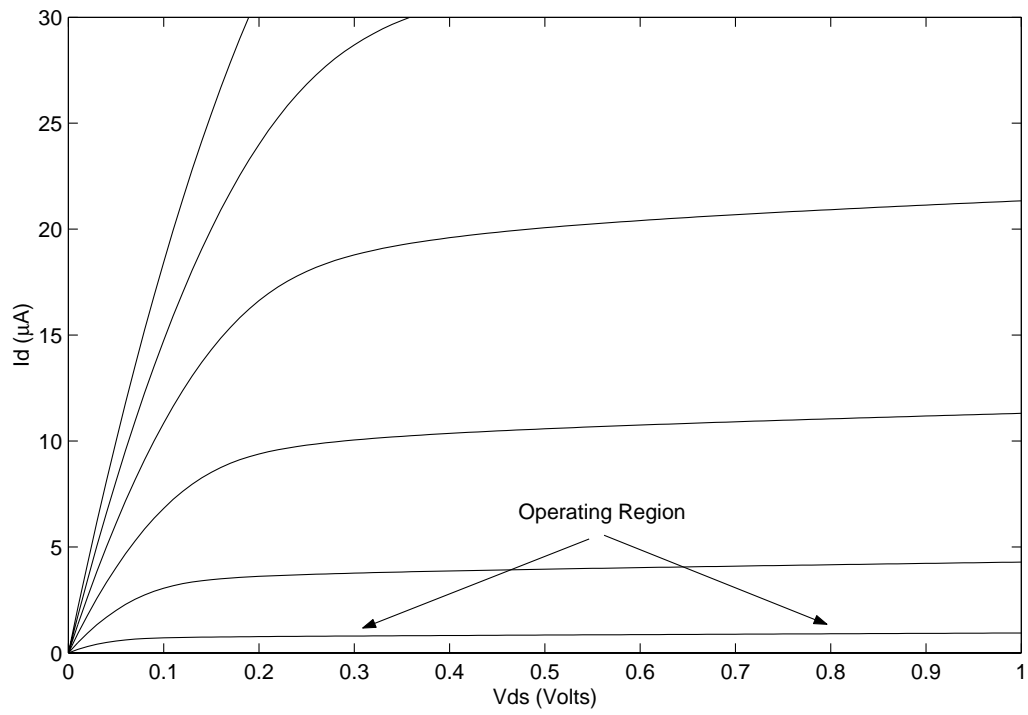 have been published that show static performance at the 10-Bit level with a die size as small as what was presented. A brief summary of the thoughts and ideas presented in this work is given followed by a short discussion on future work that can be done in this area.

7.1 Summary

This thesis describes the design, modeling, and implementation of two area efficient highly accurate DC DACs. The presented 10-Bit DAC uses the performance advantages of thermometer coding on the 3 most significant bits, while maximizing performance and minimizing area with a R-2R ladder for the least significant bits. An ultra high gain servoing technique was used to overcome the limitations of the 1.8V power supply. This technique was used to design a linear current mirror with 1 V of available headroom at the output.

An advanced MATLAB model was presented that analyzed the branch currents in various DAC designs, and allowed for a side-by-side comparison of architectures. This model was used to assign random device mismatch and observe which architectures showed the best performance. The MATLAB model showed the drastic improvement in performance with a resistor based design over a standard current steering design without resistors for the given mismatch parameters.

A five stage, ultra high gain op-amp with feed-forward parallel path compensation was presented for servoing. The op-amp has a loop gain of 130 dB and a

loop phase margin of 81°. The feed-forward op-amp was extensively modeled with MATLAB to produce pole/zero locations and accurately predict the AC response. The model allowed for a complete analysis of the op-amp response to variations in device parameters.

The 10-Bit DAC described in chapter 3 was fabricated in a standard digital, 0.18 μm CMOS process. Special attention was given to the layout to minimize the effects of process and temperature gradients. MATLAB and SPICE modeling lead to an accurate DC DAC which has been optimized for area. The layout measures 110 μm $\times$ 94 μm, and consumes 0.0104 mm^2 of area. The measured results show extremely promising figures for such a compact and efficient DAC. The measurements correlate very well with the simulated results presented. The maximum measured INL is 1.65 LSBs and the maximum measured DNL is -0.95 LSBs; proving that the fabricated DAC is 10-Bit monotonic.

7.2 Future Research

New theories and ideas are constantly surfacing which attempt to improve the performance of mixed-signal ICs. Improvements in continuous time op-amp offset cancellation could be applied directly to the designs presented in this work. An area efficient method for canceling offsets in the servoing op-amps would improve the performance of the output current mirror. In addition, canceling the offset in the servo op-amps added in the 13-Bit design would eliminate the need for a cascode current source. Using a single device current source would allow the 10-Bit core to have more headroom while operating in the 13-Bit design, and hence would improve its performance. Modeling of the 13-Bit design could be extended into MATLAB the same way the 10-Bit design was. Additional MATLAB modeling of the 10-Bit design could also include the second order effects of the cascode current sources, and

the non-linear resistance created by the switches. And finally, the size of the current source array in the DAC could be extended to achieve better matching, or the DAC could be implemented in a different process where the matching characteristics are more accurately controlled.

REFERENCES

1. S.-Y. Chin and C.-Y. Wu, "A 10-b 125-MHz CMOS Digital-to-Analog Converter with threshold voltage compensated current sources," *IEEE J. Solid State Circuits*, vol. 29, pp. 1374–1380, November 1994.

2. A. V. den Bosch, M. Borremans, M. Steyaert, and W. Sansen, "A 10-bit 1-GS/s nyquist current-steering CMOS D/A converter," *IEEE J. Solid State Circuits*, vol. 36, pp. 315–324, March 2001.

3. C. Hammerschmied and Q. Huang, "Design and implementation of an untrimmed MOSFET-only 10-bit A/D converter with -79-dB THD," *IEEE J. Solid State Circuits*, vol. 33, pp. 1148–1157, August 1998.

4. B. Greenley, U.-K. Moon, and R. Veith, "A 1.8 V CMOS DAC cell with ultra high gain op-amp in 0.0143 mm^2," *Proc. of the IEEE International Symposium on Circuits and Systems*, May 2001.

5. C.-H. Lin and K. Bult, "A 10-b, 500-MSample/s CMOS DAC in 0.6 mm^2," *IEEE J. Solid State Circuits*, vol. 33, pp. 1948–1958, December 1998.

6. K. Bult and G. Geelen, "An inherently linear and compact MOST-only current division technique," *IEEE J. Solid State Circuits*, vol. 27, pp. 1730–1735, December 1992.

7. M. Borgatti, A. Rocchi, M. Bisio, M. Besana, L. Navoni, and P. Rolandi, "A 64-Min single-chip voice recorder/player using embedded 4-b/cell flash memory," *IEEE J. Solid State Circuits*, vol. 36, pp. 516–521, March 2001.

8. A. Rofougaran, G. Chang, J. Rael, J.-C. Chang, M. Rofougaran, P. Chang, M. Djafari, J. Min, E. Roth, A. Abidi, and H. Samueli, "A single-chip 900-MHz spread spectrum wireless transceiver in 1-μm CMOS part II: receiver design," *IEEE J. Solid State Circuits*, vol. 33, pp. 535–547, April 1998.

9. T. Cho, E. Dukatz, M. Mack, D. Macnally, M. Marringa, S. Mehta, C. Nilson, L. Plouvier, and S. Rabii, "A single-chip CMOS direct-conversion transceiver for 900-MHz spread spectrum digital cordless phones," *Proc. of the IEEE International Solid-State Circuits Conference*, pp. 228–229, February 1999.

10. D. Seo, A. Weil, and M. Feng, "A 14Bit, 1 GS/s digital-to-analog converter with improved dynamic performances," *Proc. of the IEEE International Symposium on Circuits and Systems*, pp. V541–V544, May 2000.

11. J. Bastos, A. Marques, M. Steyaert, and W. Sansen, "A 12-Bit intrinsic accuracy high-speed CMOS DAC," *IEEE J. Solid State Circuits*, vol. 33, pp. 1959–1969, December 1998.

12. A. V. den Bosch, M. Steyaert, and W. Sansen, "The extraction of transistor mismatch parameters: the CMOS current steering D/A converter as a test structure," *Proc. of the IEEE International Symposium on Circuits and Systems*, pp. II745–II748, May 2000.

13. V. Cheung, H. Luong, and W. Ki, "A 1-V CMOS switched-opamp switched capacitor pseudo-2-path filter," *IEEE J. Solid State Circuits*, pp. 14–22, January 2001.

14. M. Dessouky and A. Kaiser, "Very low-voltage digital-audio $\Delta\Sigma$ modulator with 88-dB dynamic range using local switch bootstrapping," *IEEE J. Solid State Circuits*, pp. 349–355, March 2001.

15. D. A. Johns and K. Martin, *Analog Integrated Circuit Design*. New York, NY: John Wiley & Sons, Inc., 1997.

16. B. Razavi, *Principles of Data Conversion System Design*. New York, NY: IEEE Press, 1999.

17. S. Norsworthy, R. Schreier, and G. Temes, *Delta-Sigma Data Converters: Theory, Design, and Simulation*. New York, NY: IEEE Press, 1997.

18. D. Mercer, "A 16-b D/A converter with increased spurious free dynamic range," *IEEE J. Solid State Circuits*, vol. 29, pp. 1180–1185, October 1994.

19. A. V. den Bosch, M. Borremans, M. Stayeart, and W. Sansen, "A 12b 500MSample/s current-steering CMOS D/A converter," *Proc. of the IEEE International Solid-State Circuits Conference*, pp. 366–367, February 2001.

20. G. V. der Plas, J. Vandenbussche, W. Sansen, M. Steyaert, and G. Gielen, "A 14-bit intrinsic accuracy Q^2 random walk CMOS DAC," *IEEE J. Solid State Circuits*, vol. 34, pp. 1708–1718, December 1999.

21. A. Bugeja, B.-S. Song, P. Rakers, and S. Gillig, "A 14-b, 100-MS/s CMOS DAC designed for spectral performance," *IEEE J. Solid State Circuits*, vol. 34, pp. 1719–1731, December 1999.

22. A. Thomsen, D. Kasha, L. Wang, and W. Lee, "A 110-dB-THD, 18mW DAC using sampling of the output and feedback to reduce distortion," *IEEE J. Solid State Circuits*, vol. 34, pp. 1733–1740, December 1999.

23. J. W. Yang and K. W. Martin, "High-resolution low-power CMOS D/A converter," *IEEE J. Solid State Circuits*, vol. 24, pp. 1458–1461, October 1989.

24. R. Eschauzier and J. Huijsing, *Frequency Compensation Techniques For Low-Power Operational Amplifiers*. Dordrecht, The Netherlands: Kluwer Academic Publishers, first ed., 1995.

25. T. H. Lee, *The Design of CMOS Radio-Frequency Integrated Circuits*. New York, NY: Cambridge University Press, 1998.

26. J. Schoeff, "An inherently monotonic 12 bit DAC," *IEEE J. Solid State Circuits*, vol. SC-14, pp. 904–911, December 1979.

27. A. Thomsen, E. Angel, S. Wu, A. Amar, and L. Wang, "A DC measurement IC with 130nV_{pp} noise in 10Hz," *Proc. of the IEEE International Solid-State Circuits Conference*, pp. 334–335, February 2000.

28. G. Palmisano, G. Palumbo, and R. Salerno, "A 1.5-V high drive capability CMOS op-amp," *IEEE J. Solid State Circuits*, vol. 34, pp. 248–252, February 1999.

29. D. Ribner and M. Copeland, "Design techniques for cascoded CMOS op amps with improved PSRR and common-mode input range," *IEEE J. Solid State Circuits*, vol. sc-19, pp. 919–925, December 1984.

30. A. Thomsen, "A 5 stage chopper stabilized instrumentation amplifier using feed-forward compensation," *Proc. of the IEEE VLSI Circuits Symposium*, pp. 220–223, June 1998.

31. P. Maulik, "Analysis of leakage current induced nonlinearity in resistor-ladder based data converters," *IEEE Transactions on Circuits and Systems II*, vol. 47, pp. 136–137, February 2000.

32. R. Adams, K. Nguyen, and K. Sweetland, "A 113-dB SNR oversampling DAC with segmented noise-shaped scrambling," *IEEE J. Solid State Circuits*, vol. 33, pp. 1871–1878, December 1998.

33. I. Fujimori and T. Sugimoto, "A 1.5 V, 4.1 mW dual-channel audio delta-sigma D/A converter," *IEEE J. Solid State Circuits*, vol. 33, pp. 1863–1870, December 1998.

34. R. Neff, P. Gray, and A. Sangiovanni-Vincentelli, "A module generator for high-speed CMOS current output digital/analog converters," *IEEE J. Solid State Circuits*, vol. 31, pp. 448–451, March 1996.

35. M. Shoji and V. Saari, "A monolithic 8-bit D/A converter with a new scheme for error compensation," *IEEE J. Solid State Circuits*, vol. sc-10, pp. 499–501, December 1975.

36. R. Suarez, P. Gray, and D. Hodges, "All-MOS charge redistribution analog-to-digital conversion techniques–part II," *IEEE J. Solid State Circuits*, vol. sc-10, pp. 379–385, December 1975.

37. H. Schouwenaars, D. Groeneveld, and H. Termeer, "A low-power stereo 16-bit CMOS D/A converter for digital audio," *IEEE J. Solid State Circuits*, vol. 23, pp. 1290–1297, December 1988.